Microporous and Mesoporous Materials 257 (2018) 222–231

Contents lists available at ScienceDirect

Microporous and Mesoporous Materials

journal homepage: www.elsevier.com/locate/micromeso

Gas adsorption and dynamics in Pillared Graphene Frameworks

Andrea Pedrielli [a, b], Simone Taioli [b, c, **], Giovanni Garberoglio [b, *], Nicola Maria Pugno [a, d, e]

[a] Laboratory of Bio-Inspired and Graphene Nanomechanics, Department of Civil, Environmental and Mechanical Engineering, University of Trento, Via Mesiano 77, 38123 Trento, Italy
[b] European Centre for Theoretical Studies in Nuclear Physics and Related Areas (ECT*-FBK), Trento Institute for Fundamental Physics and Applications (TIFPA-INFN), 38123 Trento, Italy
[c] Faculty of Mathematics and Physics, Charles University, 180 00 Prague 8, Czech Republic
[d] School of Engineering and Materials Science, Queen Mary University of London, Mile End Road, London E1 4NS, United Kingdom
[e] Ket Lab, Edoardo Amaldi Foundation, Italian Space Agency, Via del Politecnico snc, 00133 Rome, Italy

ARTICLE INFO

Article history:
Received 30 June 2017
Received in revised form
18 August 2017
Accepted 20 August 2017
Available online 31 August 2017

Keywords:
Nanomaterials
Molecular Dynamics
Gas adsorption
Porosity

ABSTRACT

Pillared Graphene Frameworks are a novel class of microporous materials made by graphene sheets separated by organic spacers. One of their main features is that the pillar type and density can be chosen to tune the material properties. In this work, we present a computer simulation study of adsorption and dynamics of H_2, CH_4, CO_2, N_2 and O_2 and binary mixtures thereof, in Pillared Graphene Frameworks with nitrogen-containing organic spacers. In general, we find that pillar density plays the most important role in determining gas adsorption. In the low-pressure regime ($\lesssim$10 bar) the amount of gas adsorbed is an increasing function of pillar density. At higher pressure the opposite trend is observed. Diffusion coefficients were computed for representative structures taking into account the framework flexibility that is essential for assessing the dynamical properties of the adsorbed gases. Good performance for the gas separation in CH_4/H_2, CO_2/H_2 and CO_2/N_2 mixtures was found, with values comparable to those of metal-organic frameworks and zeolites.

1. Introduction

In order to exploit graphene for gas adsorption and mechanical applications, many different kinds of 3D carbon-based structures were proposed in the past years, such as carbon nanotube networks [1], carbon nanoscrolls [2,3] and graphene foams [4,5]. At the same time, a growing interest was devoted to materials in which graphene is enhanced by chemical functionalization or the addition of external components such as organic molecules [6]. In this last category, Pillared Graphene Frameworks (PGF) are a novel class of materials, composed by stacked graphene layers separated by organic moieties.

Analogously to Pillared Graphene-Oxide Frameworks (PGOF) [7,8], the properties of PGFs can be varied by changing the type and density of organic spacers hence obtaining a fine tuning of gas absorption and gas separation performances. Similarly to other materials for gas adsorption such as Metal Organic Frameworks (MOFs) [9–12], Zeolitic Imidazolate Frameworks (ZIFs) [13,14] and PGOFs [15,16], the gas adsorption and separation performances of PGFs can be fruitfully studied by means of computer simulations [17].

Nevertheless, gas adsorption and separation in PGFs are still largely unexplored. In this work, we investigate these properties for a class of structures in which the spacers are nitrogen-containing organic molecules using Grand Canonical Monte Carlo (GCMC) and Molecular Dynamics (MD) simulations. The principal goal of this work is to investigate the role of pillar type and density in determining the performance of PGFs for gas adsorption. In particular, we will investigate whether the quantity of gas adsorbed or the selectivity can be optimized by varying the type and the density of pillars. In fact, one could expect adsorption to increase with the number of pillars at low pillar density (due to the presence

* Corresponding author. European Centre for Theoretical Studies in Nuclear Physics and Related Areas (ECT*-FBK), & Trento Institute for Fundamental Physics and Applications (TIFPA-INFN), 38123 Trento, Italy.
** Corresponding author. European Centre for Theoretical Studies in Nuclear Physics and Related Areas (ECT*-FBK), & Trento Institute for Fundamental Physics and Applications (TIFPA-INFN), 38123 Trento, Italy.
E-mail addresses: taioli@ectstar.eu (S. Taioli), garberoglio@ectstar.eu (G. Garberoglio).

http://dx.doi.org/10.1016/j.micromeso.2017.08.034
1387-1811/

of more adsorption sites), whereas adsorption at high pillar density could be prevented by progressive lack of available volume. Consequently, there might be a specific pillar density optimizing gas uptake.

Furthermore, the influence of pillar density and type on gas separation performances will be assessed. The gas separation performance for a gas mixture depends in general on two main factors: first, the competitive adsorption between the two gases, namely the gas selectivity; second, the difference in the diffusion coefficient of the two species. To estimate the gas separation performances of PGFs we will compute the gas selectivity for different mixtures as well as the diffusion coefficients for single component gases.

In computing the diffusion coefficients and assessing the dynamical properties of the adsorbed gases, the flexibility of the adsorbent can strongly influence the simulation results, as shown for other materials [13,18]. Due to the high mobility of the structure considered in this work, we took into account structural flexibility in all dynamical simulations.

2. Computer model

PGFs are composed by stacked graphene layers separated by organic spacers. Here we investigate a narrow class of these structures with four types of nitrogen-containing organic spacers. For each type of organic spacer we generated several computational samples with various pillar densities, between 0.09 and 1.71 pillars nm^{-2}. We report in Fig. 1 a sketch of the unit cell of a typical PGF. In Fig. 2, the four types of organic pillars considered in this work are shown.

Although these structures have not yet been synthesized, they are likely to be realized in the nearest future. The four types of pillar selected here can be considered representative of different shapes, symmetries, rigidity and steric volumes. Moreover, they present similar lengths so that the contribution to adsorption uptake related to graphene layer distance does not change, allowing a better comparison of the pillar performance.

In generating the computational supercells, we prepared a hexagonal unit cell with periodic boundary conditions containing two graphene layers with base vectors $a = b = 3.684$ nm intercalated by the organic molecules, in such a way that the pillars were alternated in their anchorage to successive graphene planes (see Fig. 1). The length of the third base vector c, perpendicular to the graphene planes, was set to accommodate the pillars, approximately 3 nm for all the pillar types. Free volume and mass density for the samples with pillar type 1 to 4 and with representative pillar density are reported in Table 1.

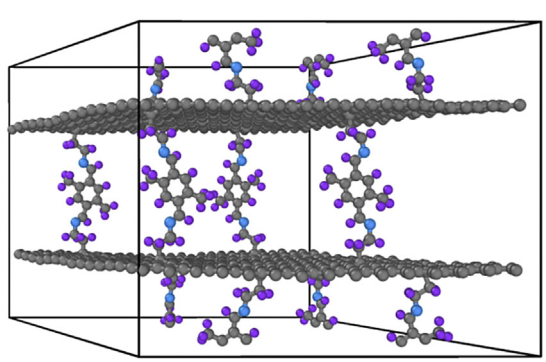

Fig. 1. Perspective view of an hexagonal unit cell of a Pillared Graphene Framework. The pillars are organic molecules covalently bonded to graphene layers. Carbon atoms are rendered in grey, hydrogen in violet and nitrogen in blue. (For interpretation of the references to colour in this figure legend, the reader is referred to the web version of this article.)

To conclude the preparation of the samples, we equilibrated them using the LAMMPS program [19] by means of 50 ps isothermal-isobaric Molecular Dynamics simulations at room conditions, using the ReaxFF potential [20,21] with parameters suitable for organic molecules and carbon-based materials [22]. For each sample, we saved one equilibrated configuration of atomic coordinates to be used in the subsequent studies. Furthermore, we saved the point charges that were self-consistently calculated during the ReaxFF simulation (QEq method [23,24]), and we used these point charges in all the simulations in which Coulomb interaction had to be taken into account.

After samples' relaxation, we computed two descriptors that are useful to characterize porous materials: Pore Size Distribution (PSD) and Accessible Surface Area (ASA). The computations were performed by means of the code Zeo++ [25,26] using the default values for atomic radii and 0.1 nm radius for the sampling sphere. The PSD is the statistical distribution of the radius of the largest sphere that can be fitted in points uniformly sampled within the pores of the material.

As an example, we report in Fig. 3 the PSD for pillar type 1; similar graphs for the other pillar types can be found in the Supplementary Information. In this plot, the PSD curves are shown for various pillar densities. The radius of the most probable pore decreases for increasing pillar density. At lower densities the main peak is around 1.2 – 1.4 nm (0.8 – 1.2 nm for pillar type 4), whereas for higher densities the peak is less intense and shifted towards 0.8 nm (0.6 nm for pillar type 4). In the limit of low pressure, smaller pores can in general store more fluid than bigger ones, due to the favorable interaction of the fluid with the pore wall.

In Fig. 4 we report the ASA as function of the pillar density, for various pillar types. The ASA is an increasing function of the pillar density, with the exception of pillar type 4. In this case, the ASA presents a maximum for intermediate pillar density and a decrease for higher pillar densities. Visual inspection of the atomic configurations shows that in this last case the pillars are tightly packed, with relative distances of the order of the size of the atoms.

To investigate gas adsorption and separation in these materials we used the Grand Canonical Monte Carlo method. For a detailed description of the method we refer the reader to a previous paper [13]. In GCMC, as well as in Molecular Dynamics simulations, it is necessary to choose a model for both the gas-gas and the gas-adsorbent interaction. Here we describe the molecules as either spherical particles or rigid linear rotors interacting via Lennard-Jones sites and point charges. In particular, we used the EPM2 potential for CO_2 [27], and the potential validated by Murthy for N_2 [28] and by Zhang [29] for O_2. In the case of CH_4 and H_2 we used a single-site Lennard-Jones potential, with the parameters validated by Buch [30] and Goodbody [31], respectively. The pure-fluid phase diagram is well described by these models.

The commonly used DREIDING [32] force field, augmented with the ReaxFF framework charges, was used to describe the gas-adsorbent interaction. Another popular choice is the UFF force field [33], which we considered for some cases. Analogously to other studies appeared in the literature, we also found that UFF generally results in higher adsorption quantities than DREIDING [34–36]. The cutoff of the long range van der Waals and Coulomb gas-adsorbent interactions was set to 1.6 nm.

Framework flexibility is known to have strong effects on molecular transport in materials with small window sizes or soft components whereas in rigid structures with large pores it has minor effects [37–40]. For the materials considered in this work the pore size as well as the structural rigidity is dependent on the pillar density so that the mobility of the adsorbent during the gas

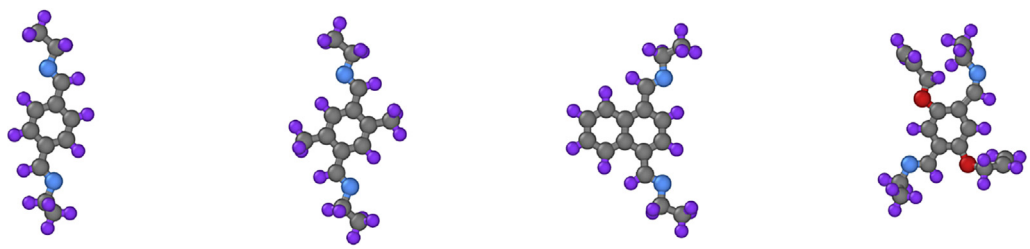

(a) Pillar type 1 (b) Pillar type 2 (c) Pillar type 3 (d) Pillar type 4

Fig. 2. The four nitrogen-containing organic pillars considered in this work. Carbon atoms are rendered in grey, hydrogen in violet, nitrogen in blue and oxygen in red. (For interpretation of the references to colour in this figure legend, the reader is referred to the web version of this article.)

Table 1
Free volume and mass density for the samples with pillar type 1 to 4 and with representative pillar density. The free volume is defined in Eq. (1).

Pillar type	Pillar density (nm^{-2})	Free volume (%)	Mass density ($g\ cm^{-3}$)
1	0.09	77.1	0.443
	0.68	67.9	0.555
	1.37	57.1	0.687
2	0.09	76.5	0.450
	0.68	65.8	0.569
	1.37	52.7	0.721
3	0.09	74.5	0.490
	0.68	65.5	0.585
	1.37	51.0	0.755
4	0.09	71.0	0.560
	0.68	55.5	0.731
	1.37	38.9	0.942

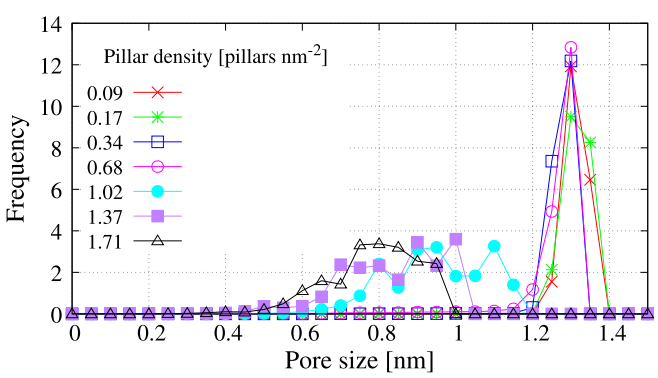

Fig. 3. Pore Size Distribution function for pillar type 1 and various pillar densities.

diffusion simulations has to be taken into account. Hence, we used the bonded part of the UFF force field to describe framework flexibility, keeping the DREIDING parameters to describe long-range dispersive interactions. Recent calculations have shown that UFF is very efficient yet capable to describe a broad range of microporous materials with reasonable accuracy [41]. Indeed, in some preliminary tests, we found that if the framework is kept rigid the diffusion coefficient can be underestimated by as much as 40%, when high pillar density structures are considered. In both GCMC and MD simulations the Lorentz–Berthelot mixing rules were used to calculate the long range van der Waals interaction between unlike atoms.

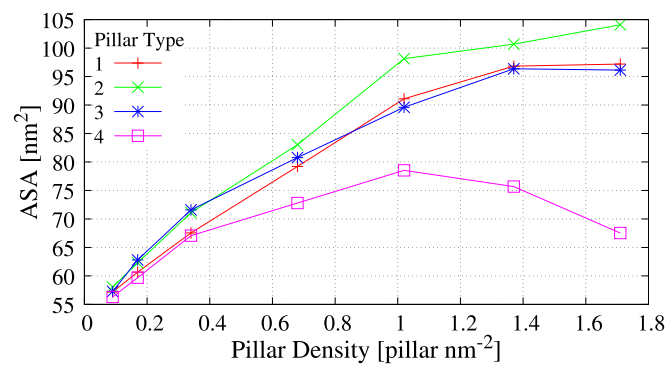

Fig. 4. Accessible Surface Area (ASA) as function of pillar density for various pillar types.

For all the simulations presented in this paper and in the Supplementary Information, the length of production run was such that the number of successful insertions were at least five times the average number of adsorbed molecules. This condition is generally deemed sufficient to assert the reliability of GCMC simulations.

3. Results and discussion

3.1. Pure-fluid isotherms

Pure fluid isotherms were computed for H_2, CH_4, CO_2, N_2 and O_2 gases. The van der Waals equation of state was used to relate the chemical potential to the pressure of the reservoir gas using parameters set to reproduce the position of the adsorbate critical point [42]. For each external pressure we performed 5×10^5 equilibration steps (one step being an insertion, a deletion, or a translation/rotation of an already adsorbed molecule, all performed with equal probabilities), followed by 1 million production steps.

In particular, we computed the excess amount, N_{ex}, that can be obtained by estimating the number density $\rho(T, P)$ of the adsorbate at the given thermodynamic condition (calculated using the van der Waals equation of state) and the available free volume for the adsorption V_{free} [42]. The free volume is conventionally defined as the volume of the region where the solid-gas interaction between the framework and a helium atom divided by the Boltzmann constant k_B is less than 10^4 K. The excess number of adsorbed molecules is then defined as

$$N_{ex} = N - \rho(T, P)\ V_{free}, \tag{1}$$

where N is the total number of gas molecules.

It is in general useful to define two kinds of isotherm curves. The first one is the volumetric isotherm which is given by the ratio between the volume occupied by the adsorbed gas at standard pressure and temperature, and the geometric cell volume. This measure of adsorption indicates how much the presence of the adsorbent can concentrate within the adsorbate with respect to room conditions. The second kind is the gravimetric isotherm and is given by the percent ratio between the weight of the adsorbed gas and the sum of the weights of the framework and the adsorbed gas. This quantity is of practical interest for fuel storage, especially for automotive applications where the weight of the system is of particular concern.

For all the gases (H_2, CH_4, CO_2, N_2, and O_2), adsorption isotherms were computed at 298 K. In the case of H_2 we also considered $T = 77$ K. In what follows, we will focus mainly on isotherms for the pillar type 1 reporting in the Supplementary Information the results for the other pillar types, because we generally found minor differences as a function of the pillar type.

Some features of these isotherms are common to almost all the cases investigated in this paper. Referring to the volumetric adsorption isotherm of CH_4 at 298 K reported in Fig. 5, one notices that at low pressures (roughly below 10 bar) the quantity of gas adsorbed increases up to two times with increasing pillar density. Indeed, visual inspection of the GCMC configurations shows that in this regime gas is mostly adsorbed close to the framework atoms and a larger number of pillars provides more adsorption sites. This trend was found for all gases except H_2 at 298 K, independently of the pillar type.

Conversely, for larger pressures, the amount of gas adsorbed is a decreasing function of the density of pillars. In this regime, the gas is also adsorbed in the volume between the pillars, but the volume available for adsorption decreases with increasing pillar density due to steric hindrance. Because the maximum volumetric uptake was found for the samples with lower pillar density, the maximum uptake is in general independent of pillar type. In fact, for high pressure, the maximum uptake is essentially limited by the total free volume, that decreases as the pillar density increases. A similar trend was observed for H_2 at 77 K in an experimental investigation of a closely related material, which used graphene-oxide instead of pure graphene [8].

The volumetric adsorption isotherms of H_2, reported in Fig. 6, do not follow this general picture. First of all, even at the highest pressure investigated here (100 bar) there is no sign of reaching saturation.

However, despite being in the "low-pressure regime", the dependence of the amount adsorbed with respect to the pillar density does not follow the trend observed in the case of the other gases, for one sees that there is an optimal pillar density (around 1 nm^{-2}) that optimizes adsorption, although volumetric uptake is similar (within 20%) for all the considered pillar densities. The same optimal pillar density was found for PGFs with pillar type 2 and 3. In the case of samples with pillar type 4, reported in Fig. 7, this optimal pillar density is not present and we found the uptake being a decreasing function of pillar density. This kind of behavior is related to the high pillar volume of the pillar of type 4, resulting in the lack of free volume also for low pillar density samples.

Gravimetric gas adsorption isotherms at $T = 298$ K for the various structures containing pillars of type 1 and different pillar density are shown in Figs. 8 and 9 in the case of CH_4 and H_2, respectively. In the case of CH_4 the isotherms display the same qualitative behavior observed in the volumetric case: adsorption increases with pillar density for low pressures, and decreases at higher ones. However, in this case the normalization with the total mass of the system enhances the difference in adsorption at high pressures, while diminishing it in the low-pressure regime.

For H_2 gravimetric isotherms, reported in Fig. 9 at 298 K we found, as usual, a linear trend up to 100 bar, so that saturation is not reached. Analogously to methane, when the adsorption per unit mass is considered, higher-density adsorbents are penalized, and in this case the best performance is observed in the lighter structure, independently of the pillar type.

Among the gases considered in this work CH_4, CO_2 and H_2 are those of major technological interest. We summarize in Tables 2 and 3 the maximum values of gravimetric and volumetric uptake found for these gases at 1, 10 and 35 bar, indicating at which pillar type and pillar density corresponds the maximum uptake.

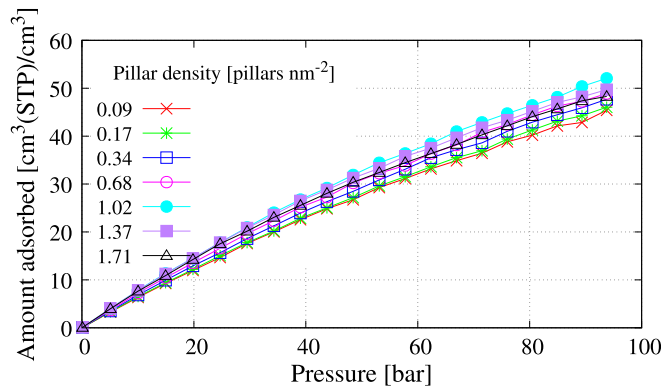

Fig. 6. Volumetric adsorption isotherms of H_2 at T = 298 K for pillar type 1. The best uptake is obtained for an intermediate pillar density of 1.02 pillars nm^{-2}.

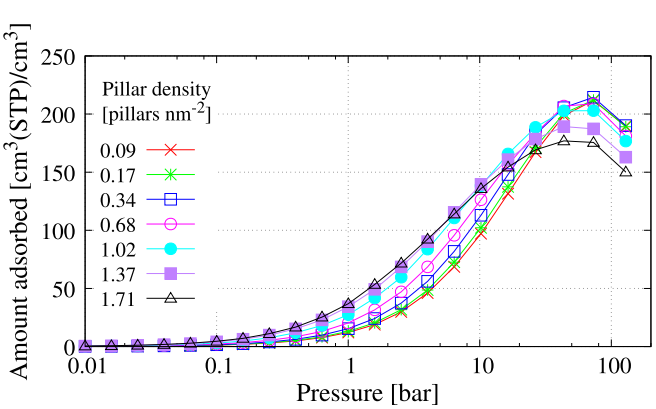

Fig. 5. Volumetric adsorption isotherms of CH_4 at T = 298 K for pillar type 1.

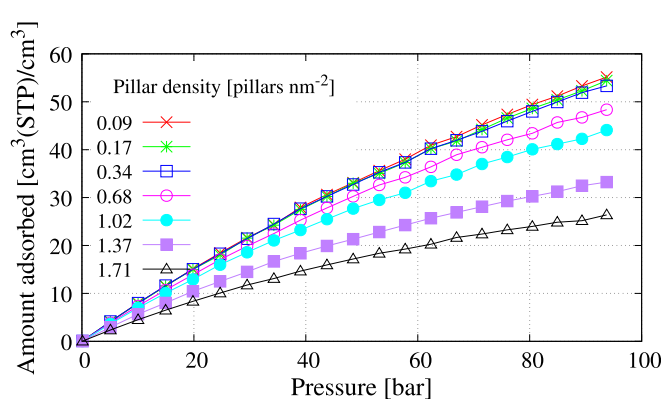

Fig. 7. Volumetric adsorption isotherms of H_2 at T = 298 K for pillar type 4. As the pillar density decreases the adsorption uptake increases.

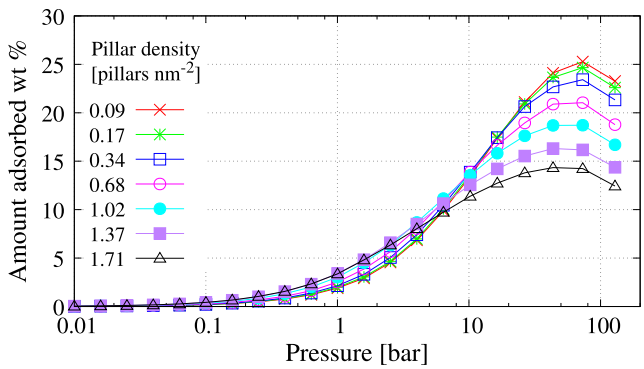

Fig. 8. Gravimetric adsorption isotherms of CH_4 at T = 298 K for pillar type 1. At high pressure, near the saturation limit, we found a clear performance decrease as pillar density increases, the contrary happens at low pressure.

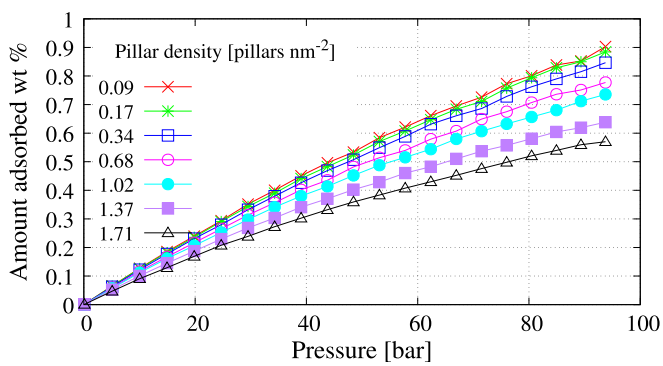

Fig. 9. Gravimetric adsorption isotherms of H_2 at T = 298 K for pillar type 1. As the pillar density decreases the adsorption uptake increases. The saturation is not reached within 100 bar.

In the case of CH_4 we found a maximum volumetric uptake at 35 bar of 195 cm^3(STP)/cm^3, with similar performances for different pillar types. This value is comparable with what is observed in MOFs, where methane uptake at the same pressure range is ≈230 cm^3(STP)/cm^3 for the best performer [43]. The performance of the well-known MOF-5 (IRMOF-1) at the same conditions is ≈150 cm^3(STP)/cm^3.

The amount of CO_2 adsorbed in PGFs is also comparable to what is found in other microporous materials, such as MOFs, where gravimetric adsorption in the range 30–74.2% is reported at room temperature and pressures up to 50 bar [35]. The maximum uptake of CO_2 for the PGFs examined is reported in Table 3 and can be up to 58.9% at 35 bar in the case of pillar type 3 at the lowest pillar density.

With regards to H_2 we found a maximum value of ≈25 cm^3(STP)/cm^3 for volumetric uptake at 35 bar (Table 2) comparable with that of small pore structures such as ZIF-9 and MOF-5 [13,34]. The value for gravimetric maximum uptake of 0.4% at 35 bar, reported in Table 3 is slightly higher than that of MOF-5 and very similar to that of IRMOF-14 [34].

Table 3
Maximum values of gravimetric uptake found for CH_4, CO_2 and H_2 at 1, 10 and 35 bar. For each pressure in the last two columns are indicated the pillar type (T) and pillar density (D) producing the maximum uptake.

	1 bar			10 bar			35 bar		
	uptake (wt%)	T	D (nm^{-2})	uptake (wt%)	T	D (nm^{-2})	uptake (wt%)	T	D (nm^{-2})
CH_4	3.76	2	1.37	15.2	4	0.09	22.3	3	0.09
CO_2	22.3	3	1.37	53.5	3	0.09	58.9	3	0.09
H_2	0.013	3	0.09	0.13	3	0.09	0.40	1	0.09

3.2. Comparison between DREIDING and UFF force fields

As already mentioned, the two force fields that are mostly used to estimate dispersion interactions between adsorbed gases and microporous organic materials are DREIDING and UFF, the latter generally resulting in a higher uptake. In order to compare the results obtained by these two force fields in PGFs, we computed

$$R(P) = \frac{N_{ex(UFF)}(P) - N_{ex(DREIDING)}(P)}{N_{ex(DREIDING)}(P)}, \quad (2)$$

where $N_{ex(UFF)}$ and $N_{ex(DREIDING)}$ are the excess number of adsorbed molecules at pressure P obtained using UFF force field and DREIDING, respectively. This quantity measures how much adsorption depends on the choice between these two force fields, and is expected to be positive on the basis of the evidence published in literature [34–36].

The values of $R(P)$ in the case of adsorption of CH_4 at 298 K temperature for all the pillar types and three different pillar density are reported in Fig. 10, where one can immediately see that also in the case of PGFs UFF predicts a larger amount of gas adsorbed than

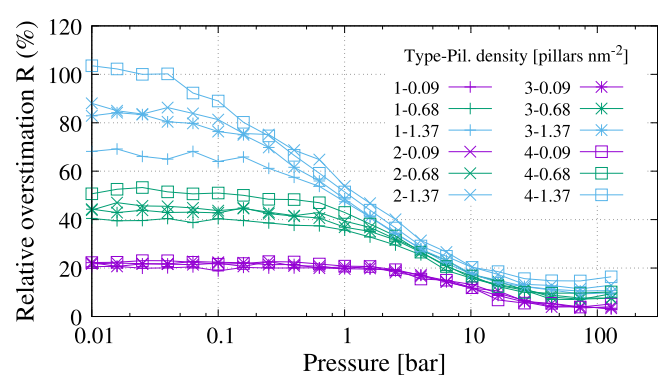

Fig. 10. Relative overestimation R of CH_4 adsorption at 298 K using UFF force field in place of DREIDING force field.

Table 2
Maximum values of volumetric uptake (cm^3(STP)/cm^3) found for CH_4, CO_2 and H_2 at 1, 10 and 35 bar. For each pressure in the last two columns are indicated the pillar type (T) and pillar density (D) producing the maximum uptake.

	1 bar			10 bar			35 bar		
	uptake (cm^3(STP)/cm^3)	T	D (nm^{-2})	uptake (cm^3(STP)/cm^3)	T	D (nm^{-2})	uptake (cm^3(STP)/cm^3)	T	D (nm^{-2})
CH_4	43.6	2	1.71	147	4	0.34	195	1	1.02
CO_2	114	2	1.71	341	4	0.09	360	3	0.09
H_2	0.81	2	0.09	8.03	2	0.09	24.6	2	0.09

DREIDING. The various curves present some clear trends. In particular, $R(P)$ is a decreasing function of the external pressure, reaching values less than 20% at saturation, and an increasing function of pillar density. This is particularly evident at low pressures ($\lesssim$10 bar), where UFF predicts up to twice as much adsorbed amount than DREIDING. In fact, adsorption in the low-pressure regime is mainly determined by the gas-framework interaction, so that the differences between the force fields are emphasized. Conversely, the interaction between gas molecules plays a greater role under saturation conditions (high pressures) and hence the difference due to the two force fields become less important. A similar behavior is observed for CO_2 at 298 K and H_2 at 77 K. Plots corresponding to Fig. 10 can be found in the Supplementary Information.

In the case of H_2 at 298 K instead (Fig. 11), $R(P)$ is essentially constant over the whole pressure range, maintaining the dependence on the pillar type and the pillar density found for the previous cases. This can be explained by the fact that the saturation regime is not reached for H_2 at 298 K, hence the decrease of $R(P)$ at high pressure that is observed in the other gases does not appear in this case.

To investigate in more detail the origin of the observed differences between these two force fields, we computed zero-coverage isosteric heat $Q_{st}^{(0)}$ in both cases. The results for CH_4, CO_2, and H_2 are reported in Fig. 12 for the PGF with pillar 4. The difference between the values obtained for the two force fields, of the order of 10%, does not explain the magnitude of the relative overestimation $R(P)$ in zero-pressure limit, which can be up to 100%, as reported in Fig. 10. This discrepancy can be explained by the fact that the isosteric heat is not the only quantity contributing to adsorption. In fact, the uptake is also proportional to the amount of volume in the cell where the solid-fluid interaction is favorable. This can be quantified by computing the Volume Density of States (VDOS), $D(E)$, which is defined so that $D(E)dE$ is the volume of space available to an adsorbate molecule at adsorption energies between E and $E + dE$.

In Fig. 13 we report the VDOS of CH_4 for the PGF with pillar 4 at the highest pillar density. The integral of the VDOS weighted with the Boltzmann factor up to the observed value of $Q_{st}^{(0)}$ is proportional to the amount of gas adsorbed at low pressures. We report this integral in Fig. 14 where we evidence the value obtained using $Q_{st}^{(0)}$ as the upper limit. In the case of the UFF force field, this quantity turns out to be almost twice as that obtained using DREIDING. In summary, both $Q_{st}^{(0)}$ and the VDOS must be considered to explain the discrepancy in the adsorption uptake between these two different force fields.

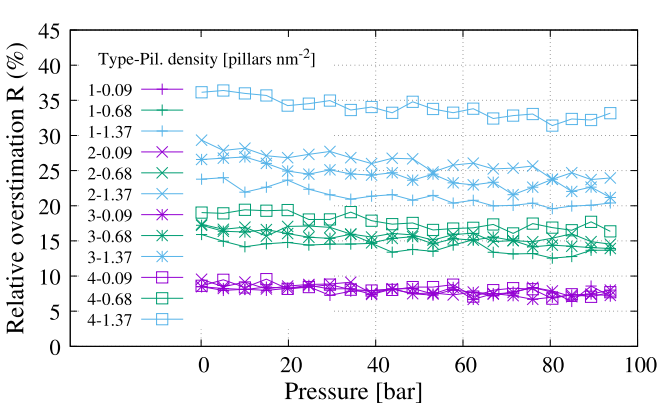

Fig. 11. Relative overestimation R of H_2 adsorption at 298 K using UFF force field in place of DREIDING force field.

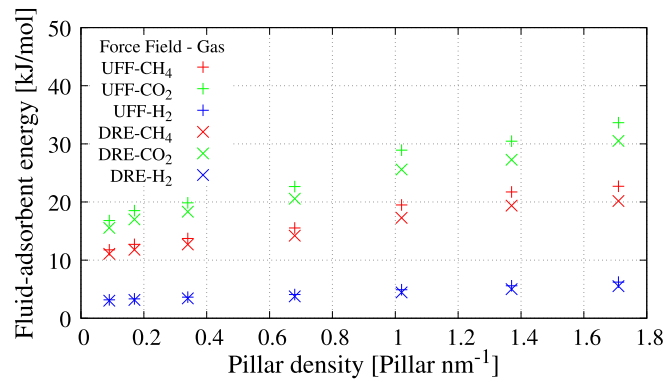

Fig. 12. Zero-coverage isosteric heat $Q_{st}^{(0)}$ for the two different force fields. The results are reported for CH_4, CO_2, and H_2 for the PGF with pillar 4.

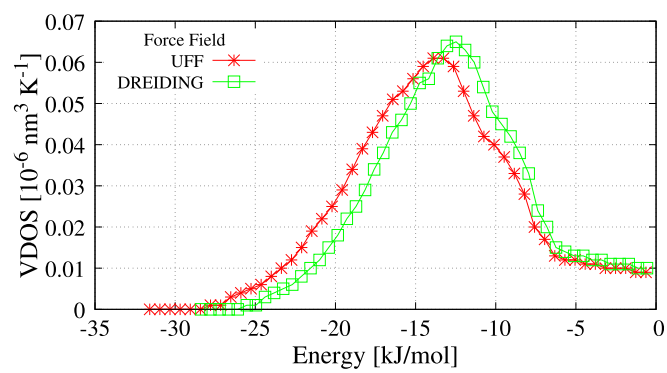

Fig. 13. VDOS for the PGF with pillar 4 and the highest pillar density, for CH_4.

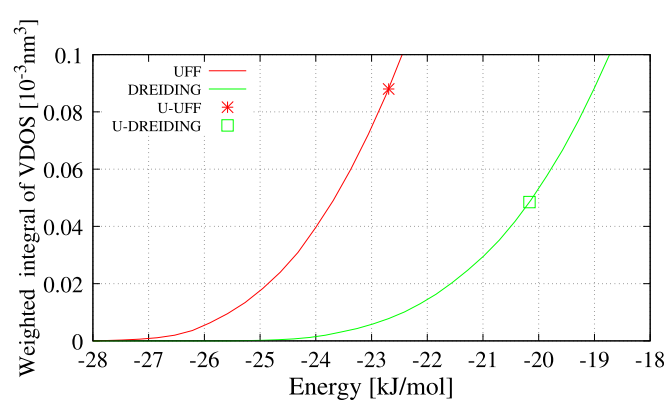

Fig. 14. Boltzmann weighted integral of VDOS for CH with UFF and DREIDING force field for PGF with pillar type 4 and highest pillar density.

The question of which force field is more suitable to describe adsorption in PGFs can be answered experimentally by performing gas adsorption measurements in the low-pressure regime where the differences between UFF and DREIDING are more pronounced.

3.3. Mixture adsorption and selectivity

We investigated the adsorption selectivity of the structures with pillar types 1 and 4 in the case of the following binary mixtures: CH_4/H_2, CO_2/H_2, CO_2/CH_4, N_2/O_2, CO_2/N_2. We chose to focus on pillar types 1 and 4 that represent the two extrema in terms of pillar complexity and pillar volume: type-1 pillar is linear and not

charged, whereas type-4 pillar has protruding charged moieties (see Fig. 2).

The selectivity of an adsorbent for a mixture of gases is defined by the ratio

$$S(b/a) = \frac{x_b/x_a}{y_b/y_a}, \tag{3}$$

where x_a, x_b denote the molar fractions of the adsorbed species a and b while y_a and y_b denote the molar fractions of the reservoir bulk mixture. In the low-pressure limit the selectivity is independent of the molar composition of the bulk gas. In this case, it can be computed as the ratio of the single-particle partition functions of the two species in the adsorbed phase, divided by the ratio of the free-particle partition functions of the same two species [13,44,45]. We denote with S_0 the low-pressure limit of the selectivity.

Values of S_0 are reported in Table 4 for pillar densities equal to 0.09, 0.68 and 1.37 pillars nm^{-2}, corresponding to the smallest, the intermediate and the higher pillar densities investigated in this work. S_0 is in general dependent on the considered mixture, the pillar density and the pillar type. Our results show that the pillar density is the most influential parameter, changing the selectivity up to a factor of almost ten. Conversely, modification of the pillar type results usually in a more modest variation of the selectivity, in the range of 50%.

The zero-pressure selectivity increases with the pillar density for all mixtures, except N_2/O_2 for which it is almost constant. The values of the selectivity for these mixtures are generally comparable to the values reported for other microporous materials, such as MOFs [34,35] or ZIFs [13,46,47].

In general, adsorption selectivity in excess of 100 is considered fairly high. In the case of the structures investigated here, this is observed for the CO_2/H_2 mixture, especially at high pillar densities where we have S_0 (CO_2/H_2) $\sim$ 340. This value is higher than the one found in ZIFs ($\sim$ 275 [13]) and also in MOFs, where it reaches the value $\sim$ 100 in CuBTC and $\sim$ 12 in MOF-5 [48].

The selectivity is in general a function of many factors, such as bulk composition of the mixture and external pressure. In the following, we will focus on the dependence of the selectivity with respect to external pressure. In order to minimize the error in the computed selectivity, the amount of molecules of both species within the simulation box should be of the same order. To this end, the bulk mole fraction of specie b in a bulk mixture (b, a) was fixed to the value $1/(1 + S_0)$ where S_0 is the zero-pressure limit of the selectivity $S(b/a)$ [13]. We note that although the selectivity does depend on the value of the mole fraction, it does not generally vary dramatically [49], hence we expect our results to be valid in a wide range of conditions.

We report in Figs. 15 and 16 the pressure dependence of $S(b/a)/S_0$ for the samples with pillar type 1 and 4, respectively, with a density of 0.68 pillars nm^{-2}. As shown in Figs. 15 and 16 all the mixture selectivities are essentially constant up to 1 bar keeping their low-pressure value. Beyond a few bars we find different trends depending on the mixture: the selectivity can either increase, remain almost constant, or decrease at large pressures with a variation of roughly a factor of two.

Table 4
Zero-pressure adsorption selectivity in the Pillared Graphene Frameworks with pillar types 1 and 4 for different pillar density.

Type	1			4		
Density (nm^{-2})	0.09	0.68	1.37	0.09	0.68	1.37
CO_2/H_2	26.2	51.4	117.6	35.8	90.2	340.0
CH_4/H_2	9.6	16.2	31.7	12.7	24.6	66.6
CO_2/CH_4	2.7	3.2	3.7	2.8	3.7	5.1
CO_2/N_2	6.3	9.1	14.0	7.1	12.3	27.1
N_2/O_2	1.00	1.02	1.04	1.01	1.02	1.01

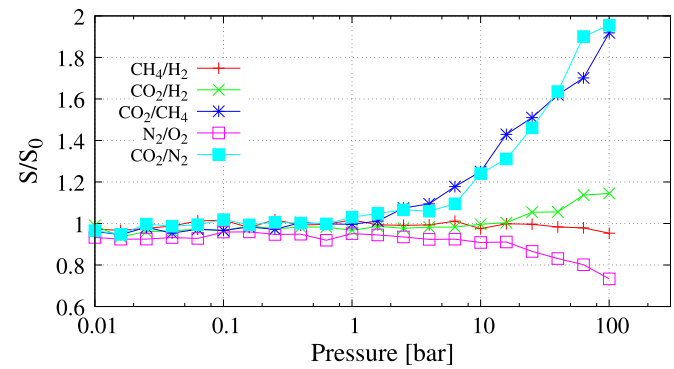

Fig. 15. Selectivity for gas mixtures at T = 298 K, normalized with respect to the zero-pressure limit value of selectivity (S_0), for the sample with pillar type 1 and pillar density 0.68 pillars nm^{-2}.

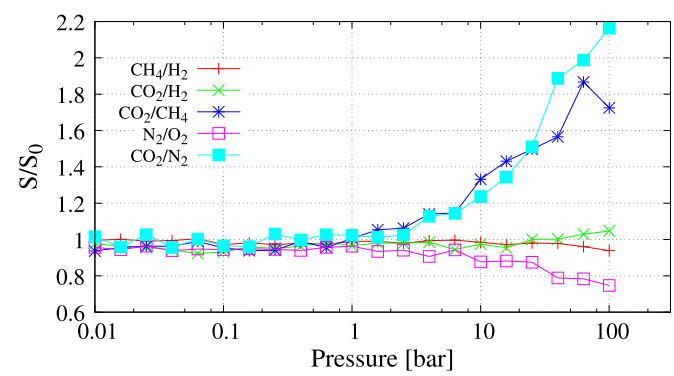

Fig. 16. Selectivity for gas mixtures at T = 298 K, normalized with respect to the zero-pressure limit value of selectivity (S_0), for the sample with pillar type 4 and pillar density 0.68 pillars nm^{-2}.

The origin of this behavior, which has also been observed in ZIFs [13] can be rationalized using energetic and entropic arguments. For molecules of the same type – e.g. both single Lennard-Jones centers such as CH_4/H_2 or linear rigid rotors such as CO_2/N_2, or N_2/O_2 – the variation in the selectivity is related to the energetic gain upon adsorption at finite pressure. In general, CO_2 is the molecule whose single-particle energy decreases the most when the adsorbed density increases. This in turn enhances the probability of another carbon dioxide molecule being adsorbed with respect to its competing species, resulting in an increasing value of the CO_2 selectivity. This is what happens for the CO_2/N_2 and CO_2/CH_4 mixtures: in both cases the energy gain upon adsorption of a carbon dioxide molecule at the highest pressure is $\sim$ 200 K larger than for the adsorption of the other one. This argument applies also in the case of N_2/O_2, where adsorption of an oxygen molecule results in roughly a 25 K gain in energy with respect to the adsorption of a nitrogen one. As a consequence, the selectivity decreases at higher pressures.

However, this picture seems to be in contrast with what is observed in the case of the CO_2/H_2 mixture, whose selectivity shows only a modest increase at the highest pressure despite the fact that CO_2 adsorption is favored by $\sim$ 100 K gain in energy. In this case one should also take into account the fact that upon adsorption, especially in packed geometries, a carbon dioxide molecule can become rotationally hindered. This loss of entropy balances the

gain of energy, resulting in a modest 20% gain in selectivity at high pressures. To check this we performed calculations at the lowest and highest pillar densities: in the former case (small hindrance) the CO_2/H_2 selectivity increases by up to 50%, in the latter it remains constant (within the uncertainties of the calculation).

3.4. Dynamics of adsorbed molecules and permeation selectivity

The simulation of gas dynamics was performed using MD within LAMMPS code [19]. The framework topologies to be used in LAMMPS code were generated according to the bonded part of UFF using a modified version of OBGMX [50]. We started from representative configuration of pure gas adsorption at two different pressures for which the adsorption uptake was maximum and half maximum. For H_2 at 298 K we take as maximum the 100 bar point.

The isothermal simulations started with a 500 ps equilibration at T = 298 K driven by a Nosé–Hoover thermostat with a time constant $\tau = 1$ ps. The x, y and z components of the mean-squared displacement were computed and averaged over 10 consecutive 500 ps MD trajectories, in which the thermostat coupling time was reduced to $\tau = 50$ ps.

The diffusion coefficients were calculated by means of a weighted least square fit of 100 ps separated points of the averaged mean-squared displacement curve. Indeed the diffusion coefficient can be computed from the mean-squared displacement curve as

$$D_x = \lim_{t \to +\infty} \frac{1}{2} \frac{d\Delta x^2(t)}{dt}, \tag{4}$$

with an analogous definition for the y and z directions. Due to the fact that all the samples present no gas diffusion in the direction perpendicular to the graphene planes, the overall diffusion coefficient can be assessed as the average between the x and the y directions,

$$D = \frac{1}{2}(D_x + D_y). \tag{5}$$

As a first test, we checked the effect of framework flexibility on the values of the self-diffusion coefficient in Eq. (5), considering the case of CH_4 and CO_2 moving in PGFs with pillar density 0.09 and 1.37 pillars nm^{-2}, pillar type 1 and 4, at maximum and half maximum gravimetric uptake. We found a relative difference in D between mobile and fixed framework of 5 – 15 % and 30 – 40 % for pillar density 0.09 and 1.374 pillars nm^{-2}, respectively. Given these results, we decided to use a flexible model of the framework in the calculation of self-diffusion.

Diffusion coefficient for pillar types 1 and 4 with pillar density 0.09, 0.68 and 1.37 pillars nm^{-2} are reported in Table 5. The general trend is a decrease of the self-diffusion coefficient with increasing pillar density.

Furthermore, H_2 is the gas with higher diffusion values followed by CH_4, N_2 and O_2 with similar values, and finally CO_2 with the lower diffusion coefficients. This sorting is largely independent of the pillar type or density.

The diffusion coefficients reported in Table 5 are all higher than 10^{-9} m^2 s^{-1}, the order of magnitude of self-diffusion coefficient in liquids such as H_2O, so that none of the considered structures inhibits gas diffusion. However, for pillar density higher than 1.37 pillars nm^{-2}, the gas diffusion could be severely hindered. Differently from ZIFs and MOFs – in which the structures with small windows connecting the pores, such as, for example, ZIF-5 and ZIF-9 [13], can easily inhibit the gas diffusion – the diffusion is observed even at high pillar density because the pore are constituted by the free volume between mobile moieties and there are no definite windows to be crossed.

The overall performance of PGFs for gas separation is determined by a tradeoff between high adsorption selectivity (which is enhanced by high pillar densities, see Table 4) and molecular transport (which is hindered by high pillar densities, see Table 5). A quantity taking into account these two distinctive factors is the so called permeance selectivity Σ which is defined as the product

$$\Sigma = S_0 \Pi, \tag{6}$$

where S_0 is the low-pressure selectivity and Π is the ratio between the self-diffusion coefficients of the two gases [13,51,52].

The separation performance factor for pillar types 1 and 4 with pillar density 0.09, 0.68 and 1.37 pillars nm^{-2} are reported in Table 6. To compute the separation performance factor the diffusion coefficients at half maximum of gravimetric uptake were used.

As general trend the separation performance factor for a given mixture increases as the pillar density increases. We found good performances for the high pillar density samples for CO_2/H_2 and CH_4/H_2 with maximum values of 22.6 and 10.1, respectively. These values are significantly larger than those found in the analysis of gas separation in ZIFs [13] where values of 3.42 and 1.42 where observed. Inspection of the values of S_0 and Π shows that the origin of the higher performance of PGFs is mainly due to their larger value of S_0, since the ratio of the diffusion coefficient leading to Π is roughly the same for PGFs and ZIFs.

A value of $\Sigma = 8.39$ was also found for CO_2/N_2 separation. For this mixture, ZIFs were found to have a maximum value $\Sigma = 10.4$, in the case of ZIF-4 [13]. For this particular mixture, PGFs have a slightly less performing separation behavior, despite having a larger value of S_0 (27.1 versus 8.2) due to the fact that the self-diffusion

Table 5
Diffusion coefficients (in units of 10^{-8} m^2 s^{-1}) for the Pillared Graphene Frameworks with pillar types 1 and 4 for different pillar density at half maximum (H) and maximum (M) gravimetric uptake.

Type		1			4		
Density (nm^{-2})		0.09	0.68	1.37	0.09	0.68	1.37
CH_4	H	30.3	12.9	3.32	35.9	7.84	0.617
	M	14.3	6.96	2.34	10.6	4.09	0.538
CO_2	H	4.04	2.85	1.27	9.56	1.60	0.270
	M	0.941	0.696	0.360	0.825	1.34	0.113
H_2	H	219	74.3	23.6	170	38.4	4.07
	M	129	49.5	20.0	105	27.8	2.79
N_2	H	23.3	10.6	4.55	15.4	5.26	0.870
	M	6.30	3.69	1.89	4.53	2.22	0.531
O_2	H	28.5	11.7	5.48	23.1	5.88	1.13
	M	8.49	4.27	2.67	5.97	2.81	0.58

Table 6
Separation performance factor $\Sigma = S_0\Pi$ for the Pillared Graphene Frameworks with pillar types 1 and 4 for different pillar density.

Type	1			4		
Density (nm^{-2})	0.09	0.68	1.37	0.09	0.68	1.37
CO_2/H_2	0.48	1.97	6.30	2.01	3.76	22.6
CH_4/H_2	1.33	2.83	4.46	2.68	5.02	10.1
CO_2/CH_4	0.36	0.70	1.41	0.75	0.75	2.23
CO_2/N_2	1.09	2.44	3.89	4.38	3.75	8.39
N_2/O_2	0.81	0.92	0.87	0.67	0.91	0.78

coefficient of N_2 is three times higher than that of CO_2 in PGFs. In the case of ZIF-4, the value of Π turns out to be ~ 1 [13].

4. Conclusions

In this paper we presented an extensive analysis of gas adsorption and separation for nitrogen-containing Pillared Graphene Frameworks using computer simulations. In particular, we focused on the influence of the pillar type and the pillar density on the performance for gas storage and separation. We took into account the quadrupole moment of CO_2, N_2 and O_2 molecules. Furthermore, we used the self-consistent point charges extracted by ReaxFF simulations to model the Coulomb interactions between the gases and the frameworks.

Our results show that the density of pillars has a greater influence on adsorption than the pillar type. Under saturation conditions, the increase of pillar density results in a sensible decrease of the amount of gas adsorbed. Despite this shortcoming, the absolute value of the amount adsorbed is comparable to what is observed in organic frameworks (MOFsor ZIFs), although it falls short to achieving the performance of the best of them.

In the case of adsorption selectivity, we found that one can have a lot of control over the performance by varying both the pillar type and density. The actual range of variability, though, depends on the specific mixture under consideration. In the case of CO_2/H_2, the ratio between the maximum and minimum adsorption selectivity at zero-pressure (see Table 4) is more than a factor of ten. Conversely, the selectivity of the N_2/O_2 mixture is always close to one, irrespectively on the nature of the pillar considered or its density. However, selectivity is in general an increasing function of the pillar density.

When dynamical properties are considered, the effect of pillar density is very pronounced. In general we found roughly an inverse proportionality between the pillar density and the self-diffusion coefficient. This finding paves the way to the possibility of tailoring transport properties to a high degree of precision, possibly up to the ballistic regime. However, there might be issues of stability of the Pillared Graphene Structure at very low pillar densities that will have to be addressed.

Finally, when the overall separation performance Σ – which includes both adsorption and diffusion – is considered, PGFs show quite a good performance when compared with other microporous materials, especially in the case of the CO_2/H_2 and CH_4/H_2 mixtures.

Acknowledgments

We thank prof. Marco Frasconi for advice on the kind of moieties to be used as pillars. N.M.P. is supported by the European Research Council PoC 2015 “Silkene” No. 693670, by the European Commission H2020 under the Graphene Flagship Core 1 No. 696656 (WP14 “Polymer Nanocomposites”) and under the Fet Proactive “Neurofibres” No. 732344. S.T and G.G. acknowledge funding from No. 696656 WP14 “Polymer Nanocomposites” grant. Access to computing and storage facilities owned by parties and projects contributing to the Czech National Grid Infrastructure MetaCentrum provided under the programme “Projects of Large Research, Development, and Innovations Infrastructures” (CESNET LM2015042), is greatly appreciated (https://www.metacentrum.cz/en/).

Appendix A. Supplementary data

Supplementary Information related to this article can be found at http://dx.doi.org/10.1016/j.micromeso.2017.08.034.

References

[1] F. Ding, Y. Lin, P.O. Krasnov, B.I. Yakobson, Nanotube-derived carbon foam for hydrogen sorption, J. Chem. Phys. 127 (2007) 164703.
[2] G. Mpourmpakis, E. Tylianakis, G.E. Froudakis, Carbon nanoscrolls: a promising material for hydrogen storage, Nano Lett. 7 (2007) 1893–1897.
[3] V.R. Coluci, S.F. Braga, R.H. Baughman, D.S. Galvão, Prediction of the hydrogen storage capacity of carbon nanoscrolls, Phys. Rev. B 75 (2007) 125404.
[4] J.A.C. Alonso, The storage of hydrogen in nanoporous carbons, J. Mexican Chem. Soc. 56 (2012) 261–269.
[5] A. Pedrielli, S. Taioli, G. Garberoglio, N.M. Pugno, Designing graphene based nanofoams with nonlinear auxetic and anisotropic mechanical properties under tension or compression, Carbon 111 (2017) 796–806.
[6] Q. Tang, Z. Zhou, Z. Chen, Graphene-related nanomaterials: tuning properties by functionalization, Nanoscale 5 (2013) 4541–4583.
[7] G. Srinivas, J.W. Burress, J. Ford, T. Yildirim, Porous graphene oxide frameworks: synthesis and gas sorption properties, J. Mater. Chem. 21 (2011) 11323–11329.
[8] R. Kumar, V.M. Suresh, T.K. Maji, C.N.R. Rao, Porous graphene frameworks pillared by organic linkers with tunable surface area and gas storage properties, Chem. Commun. 50 (2014) 2015–2017.
[9] T. Duren, L. Sarkisov, O.M. Yaghi, R.Q. Snurr, Design of new materials for methane storage, Langmuir 20 (2004) 2683–2689.
[10] R. Babarao, Z. Hu, J. Jiang, S. Chempath, S.I. Sandler, Storage and separation of CO_2 and CH_4 in silicalite, c168 schwarzite, and IRMOF-1:a comparative study from Monte Carlo simulation, Langmuir 23 (2007) 659–666.
[11] T. Duren, Y.-S. Bae, R.Q. Snurr, Using molecular simulation to characterise metal-organic frameworks for adsorption applications, Chem. Soc. Rev. 38 (2009) 1237–1247.
[12] Y.J. Colon, R.Q. Snurr, High-throughput computational screening of metal-organic frameworks, Chem. Soc. Rev. 43 (2014) 5735–5749.
[13] A. Battisti, S. Taioli, G. Garberoglio, Zeolitic imidazolate frameworks for separation of binary mixtures of CO_2, CH_4, N_2 and H_2: a computer simulation investigation, Microporous Mesoporous Mater. 143 (2011) 46–53.
[14] L. Zhang, Z. Hu, J. Jiang, Sorption-induced structural transition of zeolitic imidazolate framework-8: a hybrid molecular simulation study, J. Am. Chem. Soc. 135 (2013) 3722–3728.
[15] J.W. Burress, S. Gadipelli, J. Ford, J.M. Simmons, W. Zhou, T. Yildirim, Graphene oxide framework materials: theoretical predictions and experimental results, Angew. Chem. Int. Ed. 49 (2010) 8902–8904.
[16] G. Garberoglio, N.M. Pugno, S. Taioli, Gas adsorption and separation in realistic and idealized frameworks of organic pillared graphene: a comparative study, J. Phys. Chem. C 119 (2015) 1980–1987.
[17] X. Wang, G. Sun, P. Chen, Three-dimensional porous architectures of carbon nanotubes and graphene sheets for energy applications, Front. Energy Res. 2 (2014).
[18] L. Zhang, G. Wu, J. Jiang, Adsorption and diffusion of CO_2 and CH_4 in zeolitic imidazolate framework-8: effect of structural flexibility, J. Phys. Chem. C 118 (2014) 8788–8794.
[19] S. Plimpton, Fast parallel algorithms for short-range molecular dynamics, J. Comput. Phys. 117 (1995) 1–19.
[20] A.C.T. van Duin, S. Dasgupta, F. Lorant, W.A. Goddard, ReaxFF: a reactive force field for hydrocarbons, J. Phys. Chem. A 105 (2001) 9396–9409.
[21] K. Chenoweth, A.C.T. van Duin, W.A. Goddard, ReaxFF:reactive force field for molecular dynamics simulations of hydrocarbon oxidation, J. Phys. Chem. A 112 (2008) 1040–1053.
[22] T.R. Mattsson, J.M.D. Lane, K.R. Cochrane, M.P. Desjarlais, A.P. Thompson, F. Pierce, G.S. Grest, First-principles and classical molecular dynamics simulation of shocked polymers, Phys. Rev. B 81 (2010) 054103.
[23] A. Nakano, Parallel multilevel preconditioned conjugate-gradient approach to variable-charge molecular dynamics, Comput. Phys. Commun. 104 (1997) 59–69.
[24] A.K. Rappé, W.A. Goddard, Charge equilibration for molecular dynamics simulations, J. Phys. Chem. 95 (1991) 3358–3363.
[25] T.F. Willems, C.H. Rycroft, M. Kazi, J.C. Meza, M. Haranczyk, Algorithms and tools for high-throughput geometry-based analysis of crystalline porous materials, Microporous Mesoporous Mater. 149 (2012) 134–141.

[26] M. Pinheiro, R.L. Martin, C.H. Rycroft, A. Jones, E. Iglesia, M. Haranczyk, Characterization and comparison of pore landscapes in crystalline porous materials, J. Mol. Graph. Model. 44 (2013) 208–219.
[27] J.G. Harris, K.H. Yung, Carbon dioxide's liquid-vapor coexistence curve and critical properties as predicted by a simple molecular model, J. Phys. Chem. 99 (1995) 12021–12024.
[28] C. Murthy, K. Singer, M. Klein, I. McDonald, Pairwise additive effective potentials for nitrogen, Mol. Phys. 41 (1980) 1387–1399.
[29] L. Zhang, J.I. Siepmann, Direct calculation of Henry's law constants from Gibbs ensemble Monte Carlo simulations: nitrogen, oxygen, carbon dioxide and methane in ethanol, Theor. Chem. Accounts 115 (2006) 391–397.
[30] V. Buch, Path integral simulations of mixed para-D_2 and ortho-D_2 clusters: the orientational effects, J. Chem. Phys. 100 (1994) 7610–7629.
[31] S.J. Goodbody, K. Watanabe, D. MacGowan, J.P.R.B. Walton, N. Quirke, Molecular simulation of methane and butane in silicalite, J. Chem. Soc. Faraday Trans. 87 (1991) 1951–1958.
[32] S.L. Mayo, B.D. Olafson, W.A. Goddard, Dreiding: a generic force field for molecular simulations, J. Phys. Chem. 94 (1990) 8897–8909.
[33] A.K. Rappé, C.J. Casewit, K.S. Colwell, W.A. Goddard, W.M. Skiff, UFF, a full periodic table force field for molecular mechanics and molecular dynamics simulations, J. Am. Chem. Soc. 114 (1992) 10024–10035.
[34] G. Garberoglio, A.I. Skoulidas, J.K. Johnson, Adsorption of gases in metal organic materials: comparison of simulations and experiments, J. Phys. Chem. B 109 (2005) 13094–13103.
[35] K. Sumida, D.L. Rogow, J.A. Mason, T.M. McDonald, E.D. Bloch, Z.R. Herm, T.-H. Bae, J.R. Long, Carbon dioxide capture in metal–organic frameworks, Chem. Rev. 112 (2012) 724–781.
[36] R.B. Getman, Y.-S. Bae, C.E. Wilmer, R.Q. Snurr, Review and analysis of molecular simulations of methane, hydrogen, and acetylene storage in metal–organic frameworks, Chem. Rev. 112 (2012) 703–723.
[37] S. Amirjalayer, M. Tafipolsky, R. Schmid, Molecular dynamics simulation of benzene diffusion in MOF-5: importance of lattice dynamics, Angew. Chem. Int. Ed. 46 (2007) 463–466.
[38] E. Haldoupis, S. Nair, D.S. Sholl, Efficient calculation of diffusion limitations in metal organic framework materials: a tool for identifying materials for kinetic separations, J. Am. Chem. Soc. 132 (2010) 7528–7539. PMID: 20450176.
[39] L. Hertag, H. Bux, J. Caro, C. Chmelik, T. Remsungnen, M. Knauth, S. Fritzsche, Diffusion of CH_4 and H_2 in ZIF-8, J. Membr. Sci. 377 (2011) 36–41.
[40] E. Pantatosaki, G. Megariotis, A.-K. Pusch, C. Chmelik, F. Stallmach, G.K. Papadopoulos, On the impact of sorbent mobility on the sorbed phase equilibria and dynamics: a study of methane and carbon dioxide within the zeolite imidazolate framework-8, J. Phys. Chem. C 116 (2012) 201–207.
[41] G. Garberoglio, S. Taioli, Modeling flexibility in metal–organic frameworks: comparison between density-functional tight-binding and universal force field approaches for bonded interactions, Microporous Mesoporous Mater. 163 (2012) 215–220.
[42] J. Hirschfelder, C. Curtiss, R. Bird Molecular Theory of Liquids and Gases, 1954.
[43] J.A. Mason, M. Veenstra, J.R. Long, Evaluating metal-organic frameworks for natural gas storage, Chem. Sci. 5 (2014) 32–51.
[44] Z. Tan, K.E. Gubbins, Selective adsorption of simple mixtures in slit pores: a model of methane-ethane mixtures in carbon, J. Phys. Chem. 96 (1992) 845–854.
[45] S.R. Challa, D.S. Sholl, J.K. Johnson, Adsorption and separation of hydrogen isotopes in carbon nanotubes: multicomponent grand canonical monte carlo simulations, J. Chem. Phys. 116 (2002) 814–824.
[46] R. Banerjee, H. Furukawa, D. Britt, C. Knobler, M. O'Keeffe, O.M. Yaghi, Control of pore size and functionality in isoreticular zeolitic imidazolate frameworks and their carbon dioxide selective capture properties, J. Am. Chem. Soc. 131 (2009) 3875–3877. PMID: 19292488.
[47] M. Prakash, N. Sakhavand, R. Shahsavari, H_2, N_2, and CH_4 gas adsorption in zeolitic imidazolate framework-95 and -100: Ab initio based grand canonical Monte Carlo simulations, J. Phys. Chem. C 117 (2013) 24407–24416.
[48] Q. Yang, C. Zhong, Molecular simulation of carbon dioxide/methane/hydrogen mixture adsorption in metal–organic frameworks, J. Phys. Chem. B 110 (2006) 17776–17783. PMID: 16956262.
[49] Y.-S. Bae, K.L. Mulfort, H. Frost, P. Ryan, S. Punnathanam, L.J. Broadbelt, J.T. Hupp, R.Q. Snurr, Separation of CO_2 from CH_4 using mixed-ligand metal–organic frameworks, Langmuir 24 (2008) 8592–8598. PMID: 18616225.
[50] G. Garberoglio, OBGMX: a web-based generator of gromacs topologies for molecular and periodic systems using the universal force field, J. Comput. Chem. 33 (2012) 2204–2208.
[51] R. Krishna, J. van Baten, Using molecular simulations for screening of zeolites for separation of CO_2/CH_4 mixtures, Chem. Eng. J. 133 (2007) 121–131.
[52] J. Liu, J.K. Johnson, Prediction of CH_4/H_2 mixture selectivity in Zn(Tbip) from computer simulations, J. Low Temp. Phys. 157 (2009) 268–276.

Supplementary Information to the paper Gas Adsorption and Dynamics in Pillared Graphene Frameworks

Andrea Pedrielli[a,b], Simone Taioli[b,c,*], Giovanni Garberoglio[b,**], Nicola Maria Pugno[a,d,e]

[a] *Laboratory of Bio-Inspired and Graphene Nanomechanics, Department of Civil, Environmental and Mechanical Engineering, University of Trento, Via Mesiano 77, 38123 Trento, Italy*

[b] *European Centre for Theoretical Studies in Nuclear Physics and Related Areas (ECT*-FBK) and Trento Institute for Fundamental Physics and Applications (TIFPA-INFN), 38123 Trento, Italy*

[c] *Faculty of Mathematics and Physics, Charles University, 180 00 Prague 8, Czech Republic*

[d] *School of Engineering and Materials Science, Queen Mary University of London, Mile End Road, London E1 4NS, United Kingdom*

[e] *Ket Lab, Edoardo Amaldi Foudation, Italian Space Agency, Via del Politecnico snc, 00133 Rome, Italy*

*Second corresponding author

**First corresponding author

Email addresses: taioli@ectstar.eu (Simone Taioli), garberoglio@ectstar.eu (Giovanni Garberoglio)

August 14, 2017

1. Pore Size Distribution

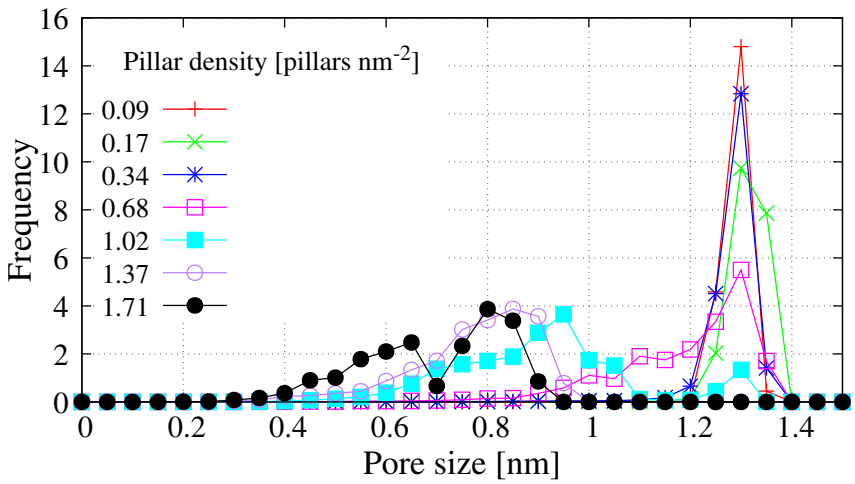

Figure 1: Pore Size Distribution for PGFs with pillar type 2 at various pillar density.

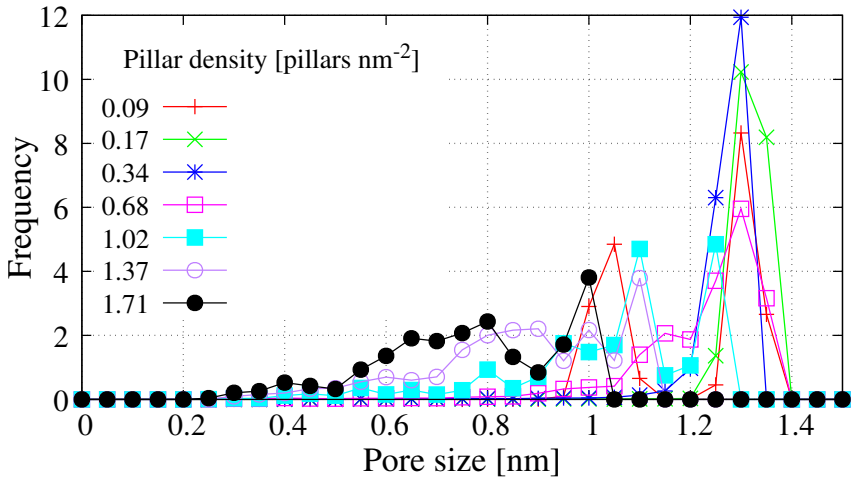

Figure 2: Pore Size Distribution for PGFs with pillar type 3 at various pillar density.

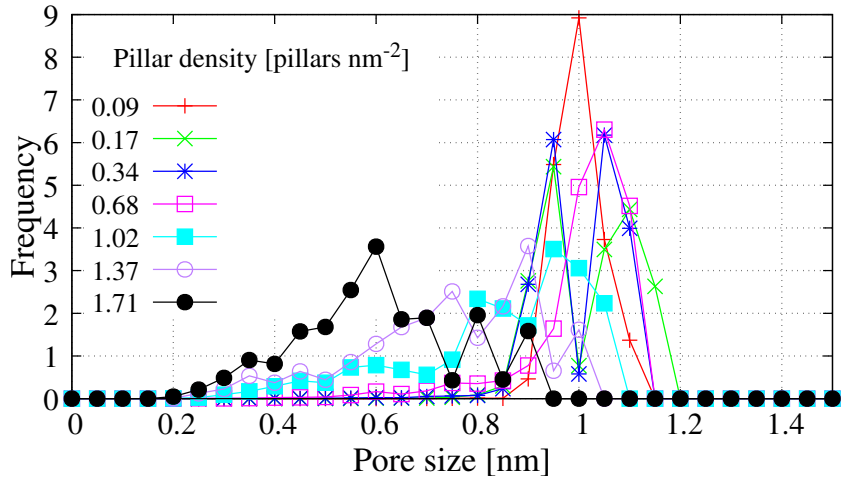

Figure 3: Pore Size Distribution for PGFs with pillar type 4 at various pillar density.

2. Adsorption isotherms (DREIDING)

2.1. Pillar type 1

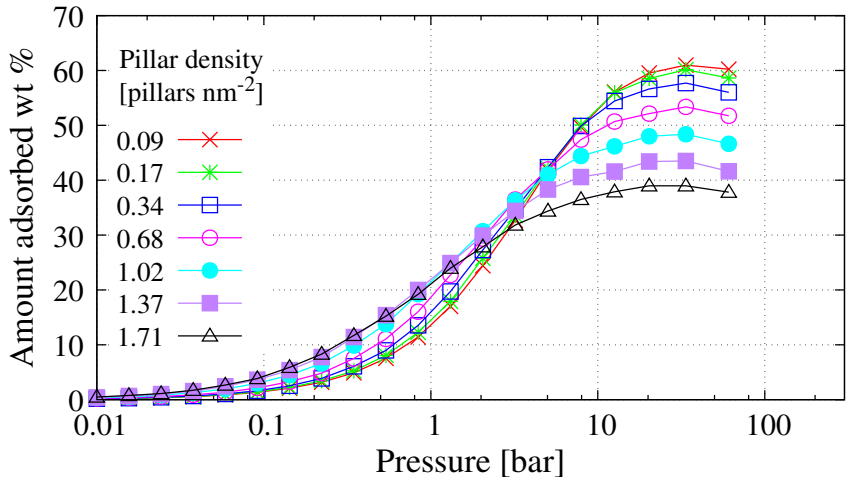

Figure 4: Gravimetric adsorption isotherms of CO_2 at T= 298 K for pillar type 1.

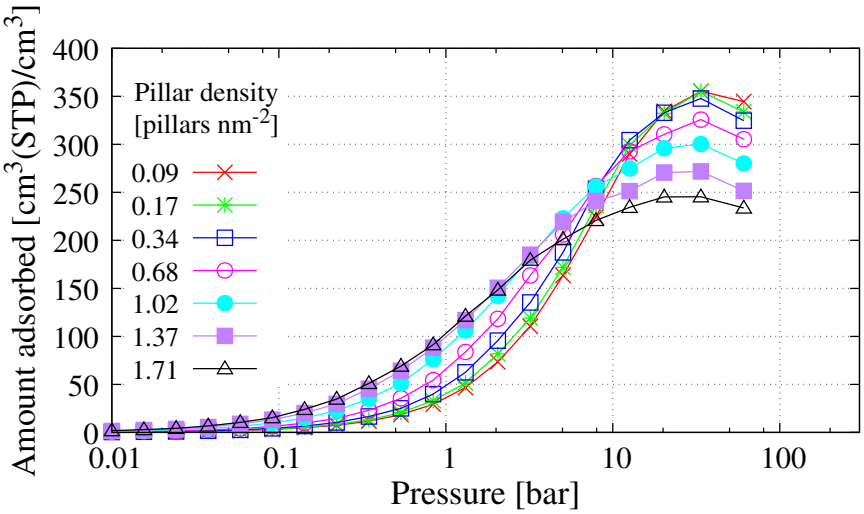

Figure 5: Volumetric adsorption isotherms of CO_2 at T= 298 K for pillar type 1.

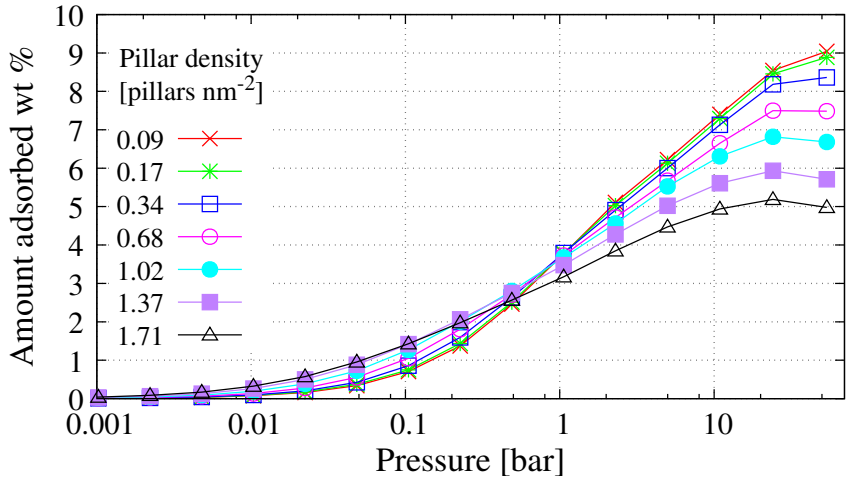

Figure 6: Gravimetric adsorption isotherms of H_2 at T= 77 K for pillar type 1.

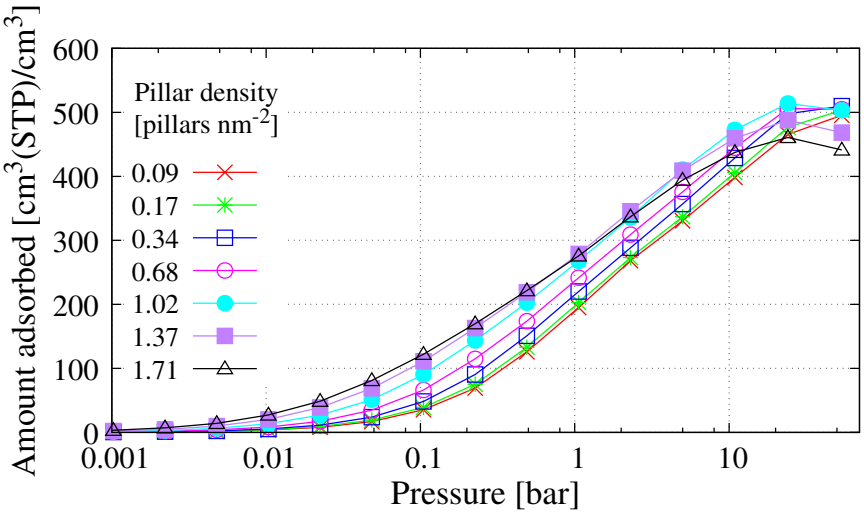

Figure 7: Volumetric adsorption isotherms of H_2 at T= 77 K for pillar type 1.

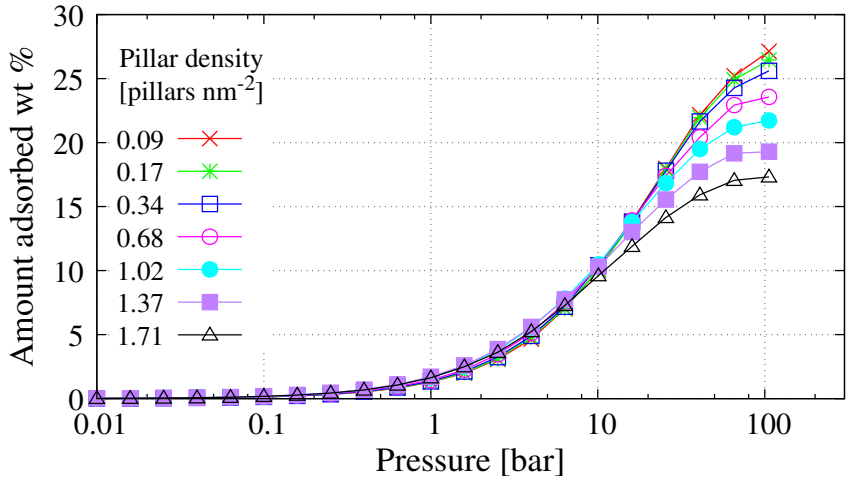

Figure 8: Gravimetric adsorption isotherms of N_2 at T= 298 K for pillar type 1.

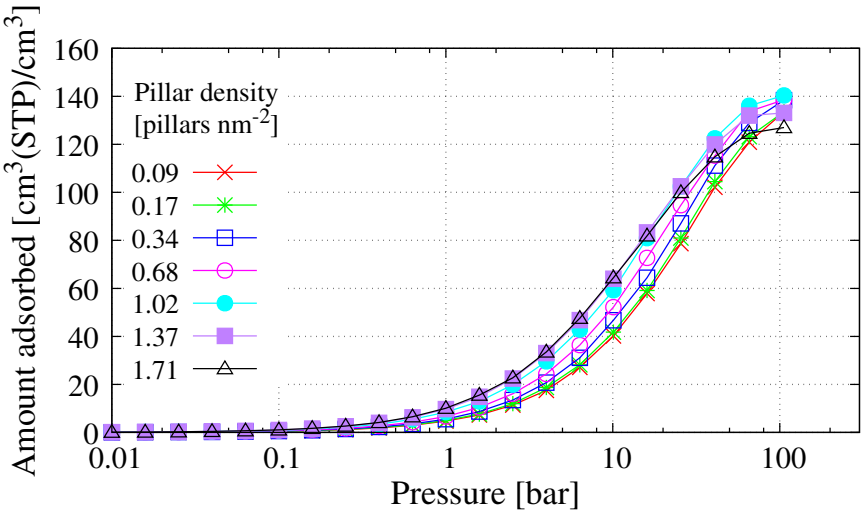

Figure 9: Volumetric adsorption isotherms of N_2 at T= 298 K for pillar type 1.

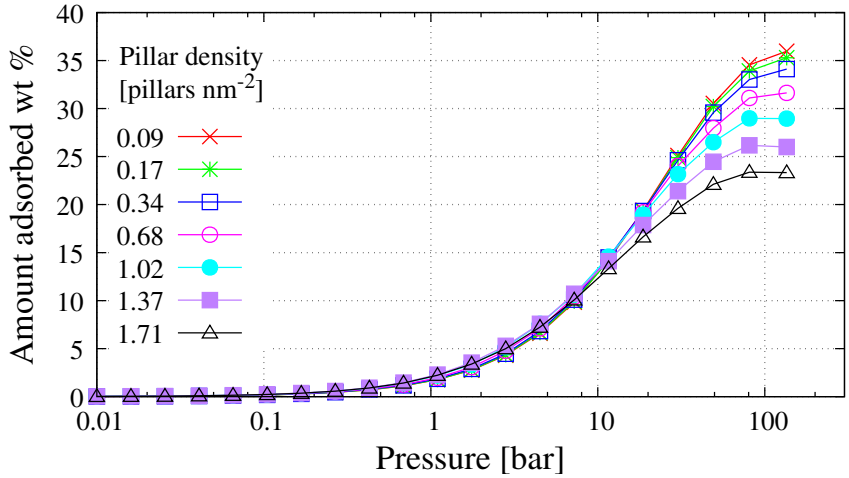

Figure 10: Gravimetric adsorption isotherms of O_2 at T= 298 K for pillar type 1.

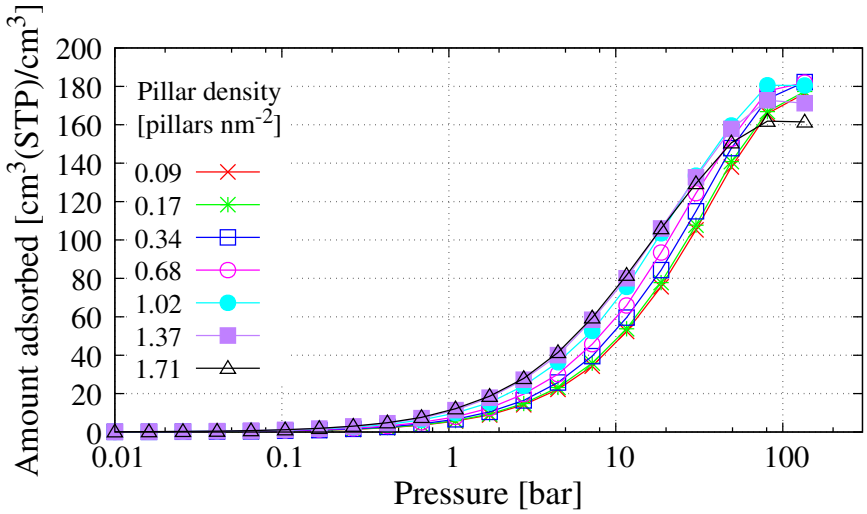

Figure 11: Volumetric adsorption isotherms of O_2 at T= 298 K for pillar type 1.

2.2. Pillar type 2

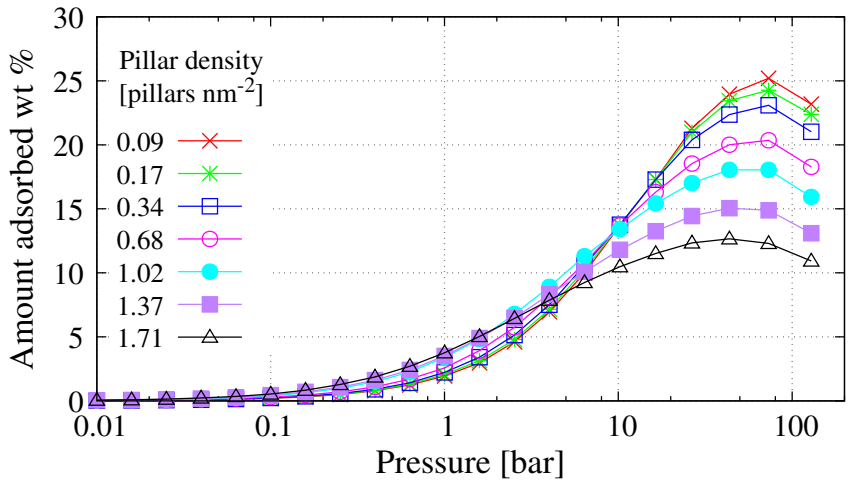

Figure 12: Gravimetric adsorption isotherms of CH_4 at T= 298 K for pillar type 2.

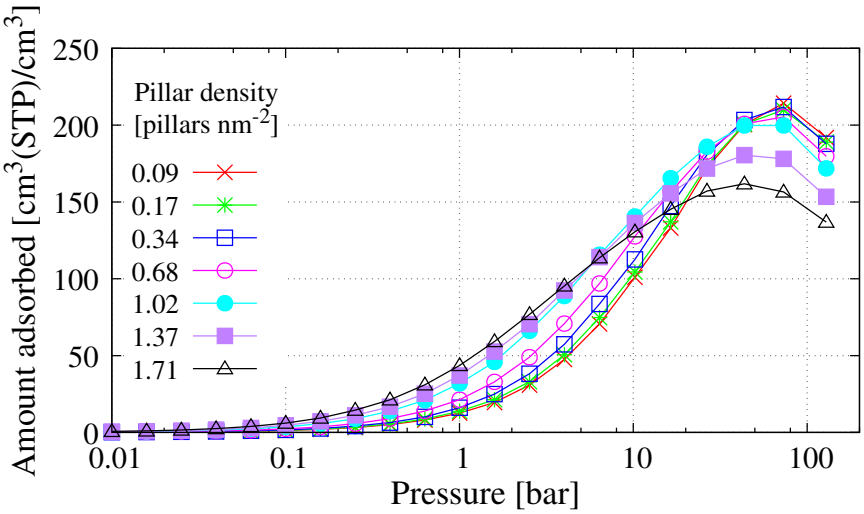

Figure 13: Volumetric adsorption isotherms of CH_4 at T= 298 K for pillar type 2.

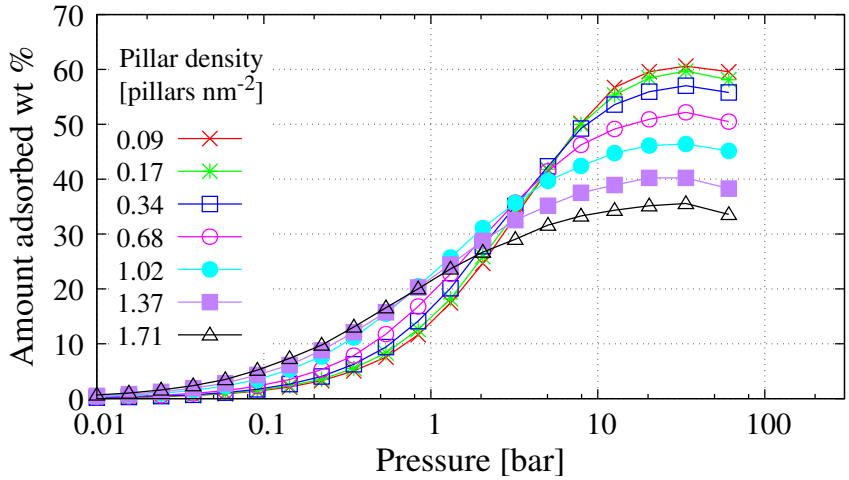

Figure 14: Gravimetric adsorption isotherms of CO_2 at T= 298 K for pillar type 2.

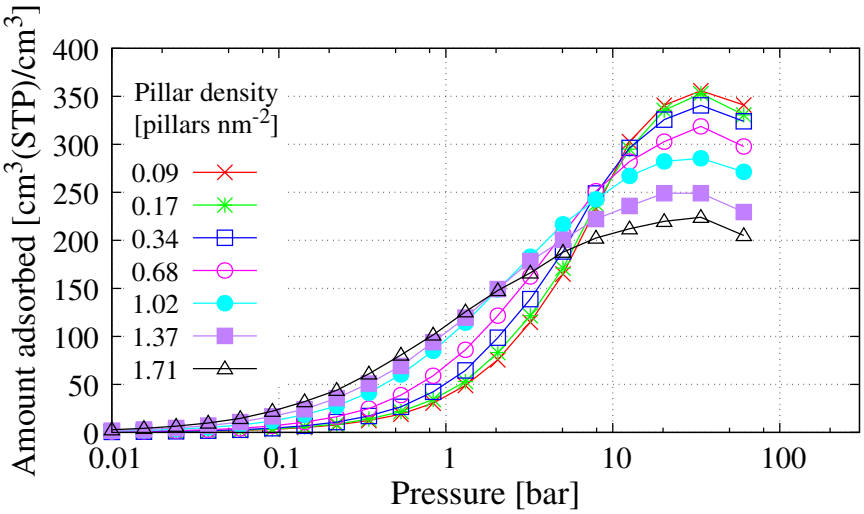

Figure 15: Volumetric adsorption isotherms of CO_2 at T= 298 K for pillar type 2.

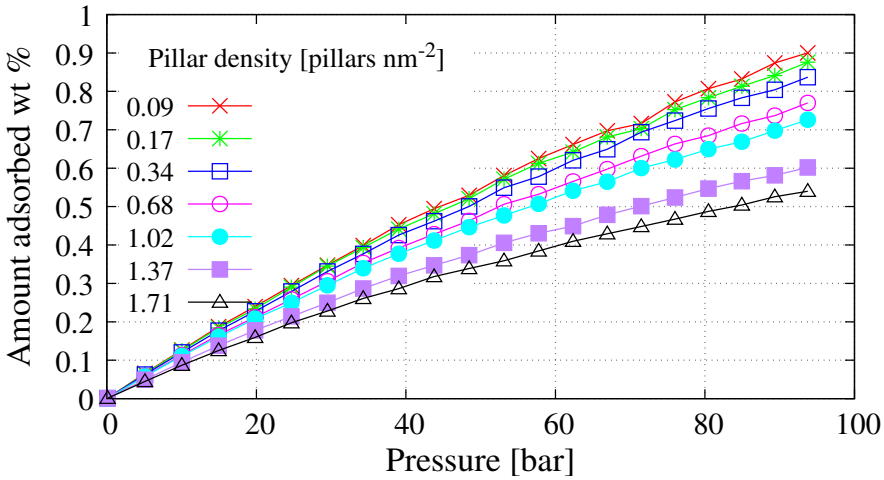

Figure 16: Gravimetric adsorption isotherms of H_2 at T= 298 K for pillar type 2.

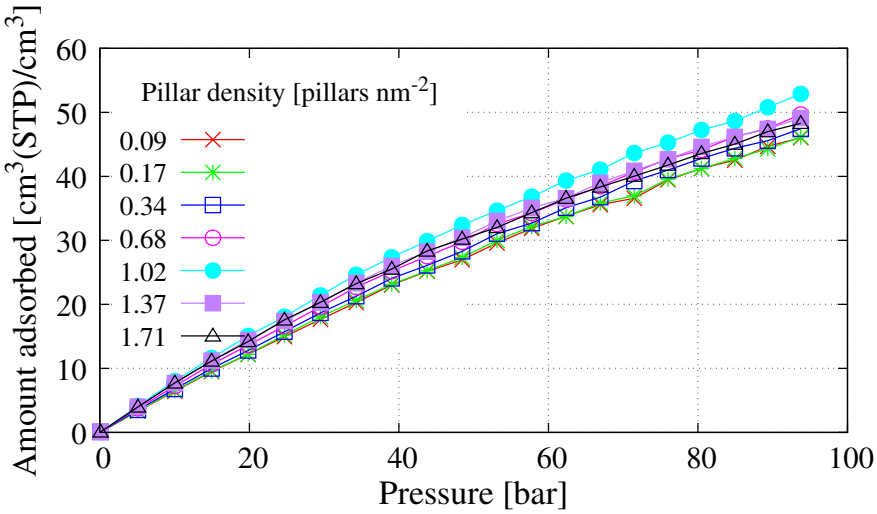

Figure 17: Volumetric adsorption isotherms of H_2 at T= 298 K for pillar type 2.

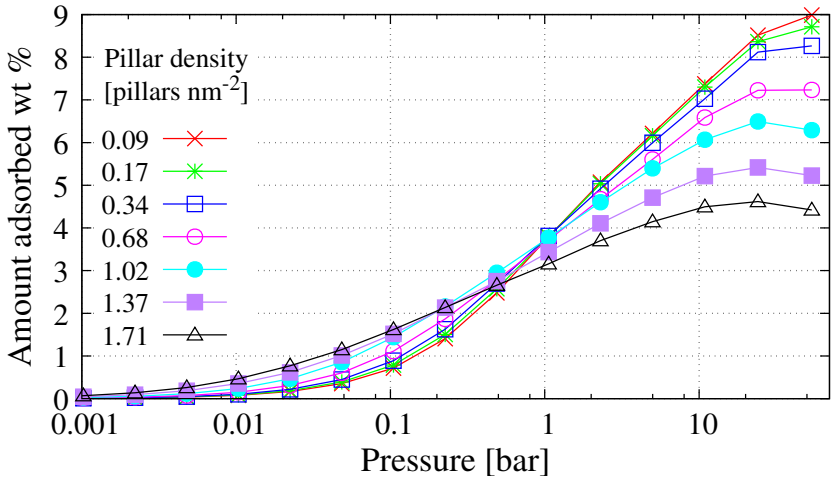

Figure 18: Gravimetric adsorption isotherms of H_2 at T= 77 K for pillar type 2.

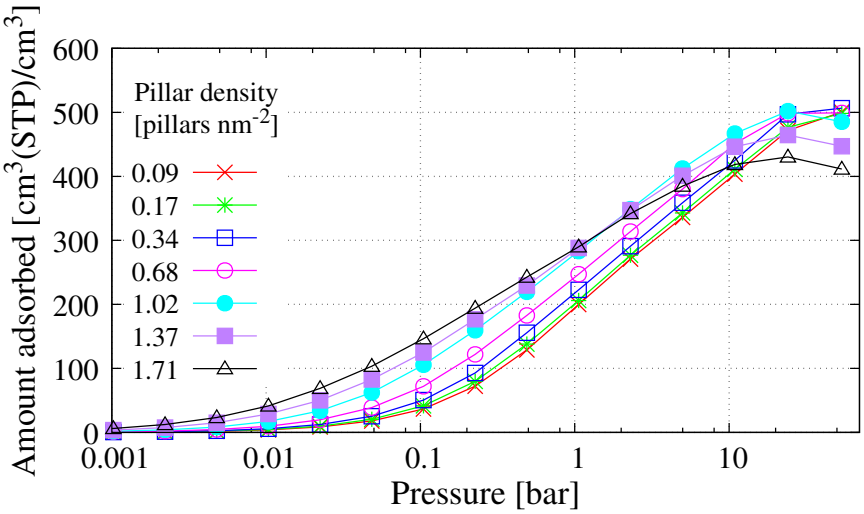

Figure 19: Volumetric adsorption isotherms of H_2 at T= 77 K for pillar type 2.

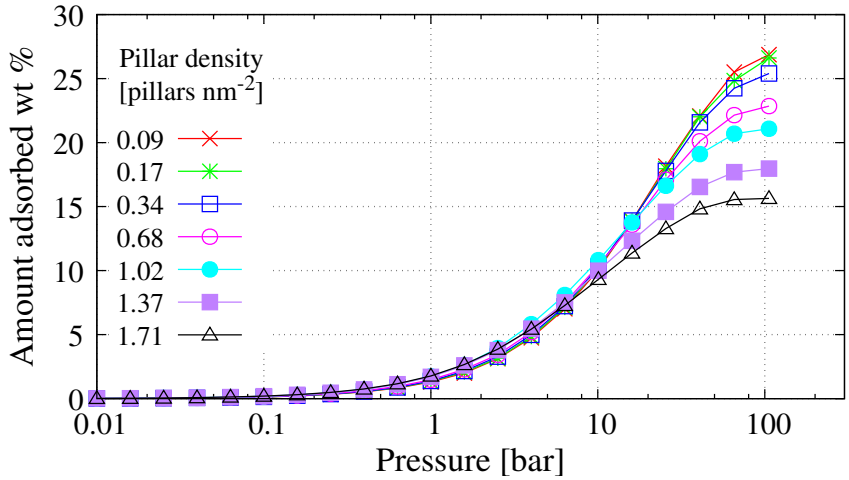

Figure 20: Gravimetric adsorption isotherms of N_2 at T= 298 K for pillar type 2.

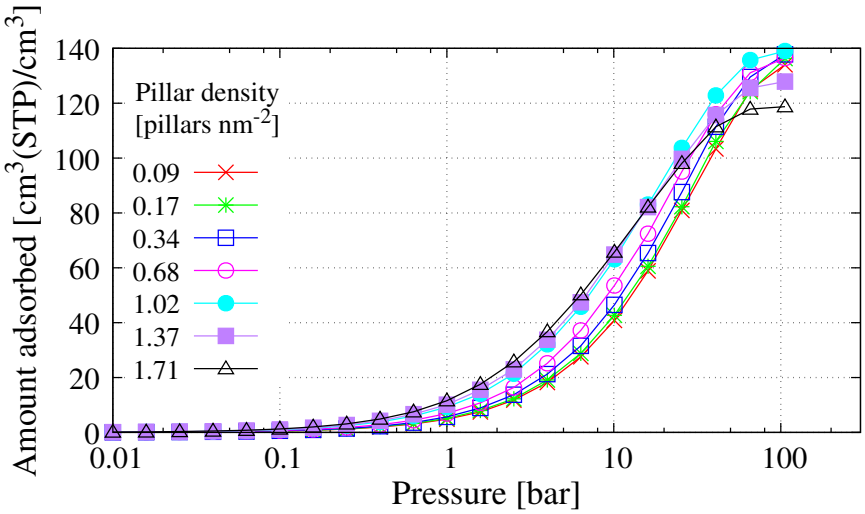

Figure 21: Volumetric adsorption isotherms of N_2 at T= 298 K for pillar type 2.

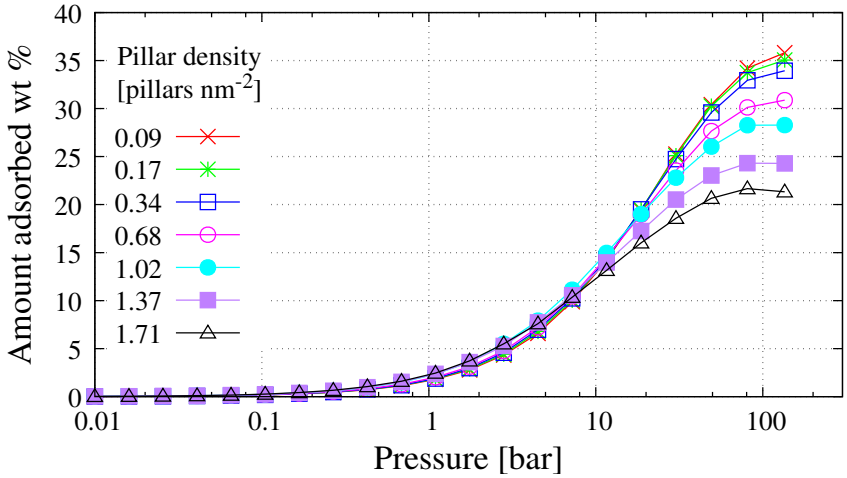

Figure 22: Gravimetric adsorption isotherms of O_2 at T= 298 K for pillar type 2.

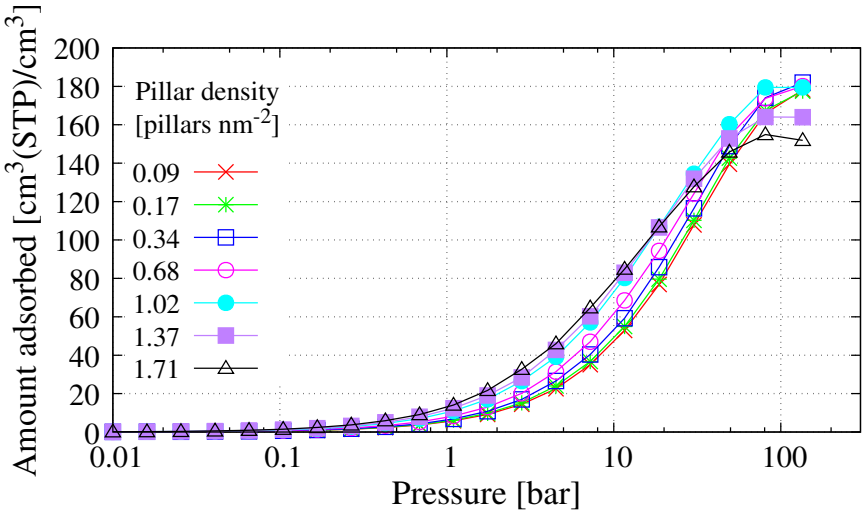

Figure 23: Volumetric adsorption isotherms of O_2 at T= 298 K for pillar type 2.

2.3. Pillar type 3

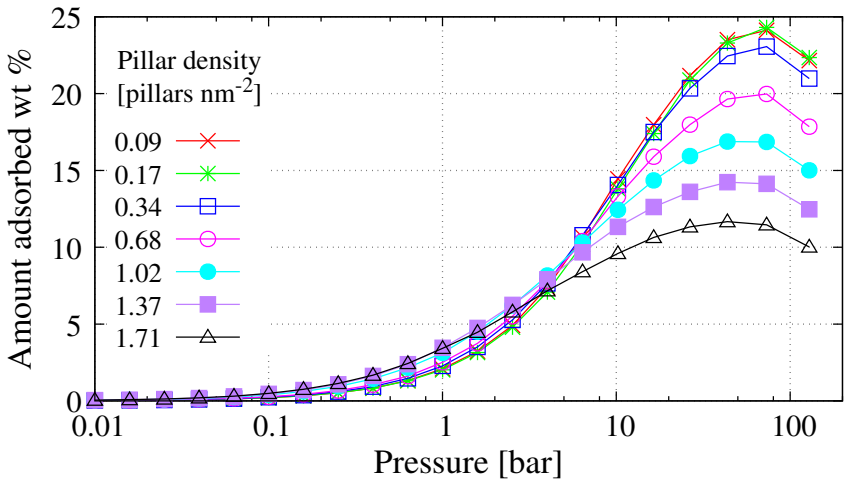

Figure 24: Gravimetric adsorption isotherms of CH_4 at T= 298 K for pillar type 3.

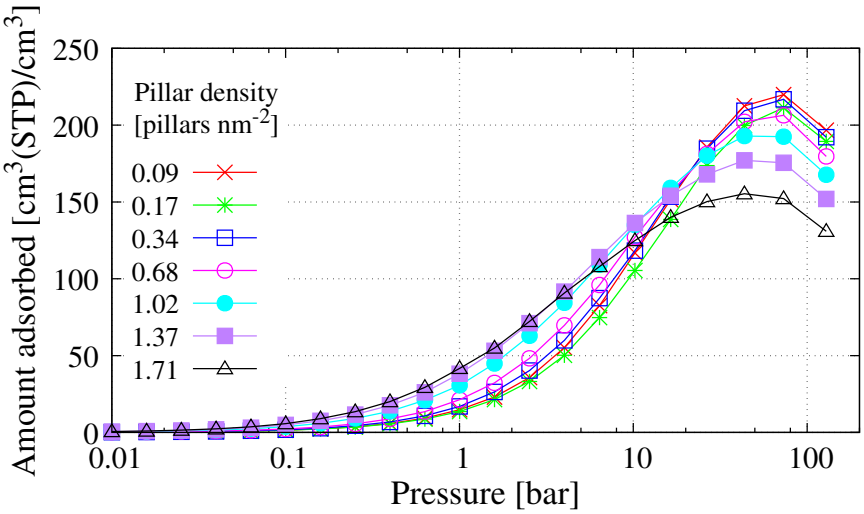

Figure 25: Volumetric adsorption isotherms of CH_4 at T= 298 K for pillar type 3.

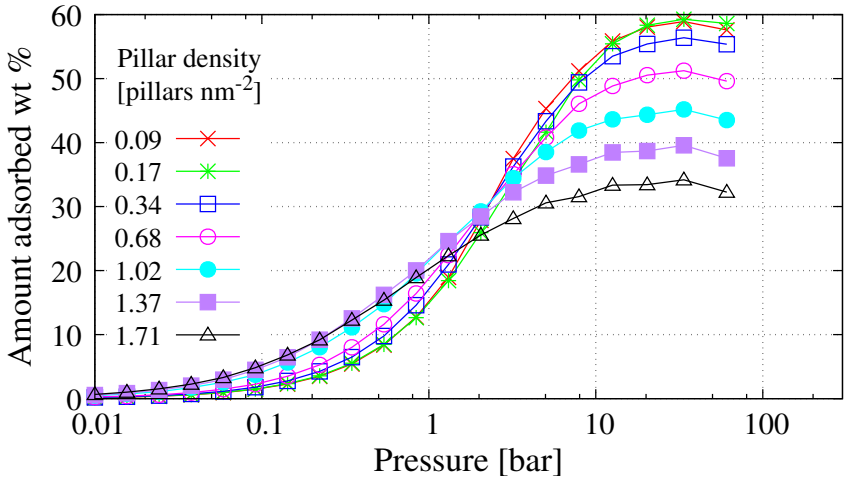

Figure 26: Gravimetric adsorption isotherms of CO_2 at T= 298 K for pillar type 3.

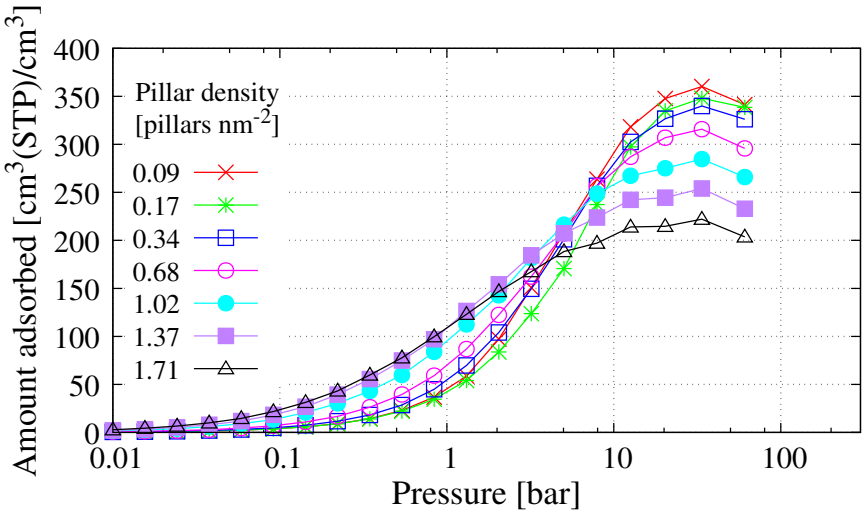

Figure 27: Volumetric adsorption isotherms of CO_2 at T= 298 K for pillar type 3.

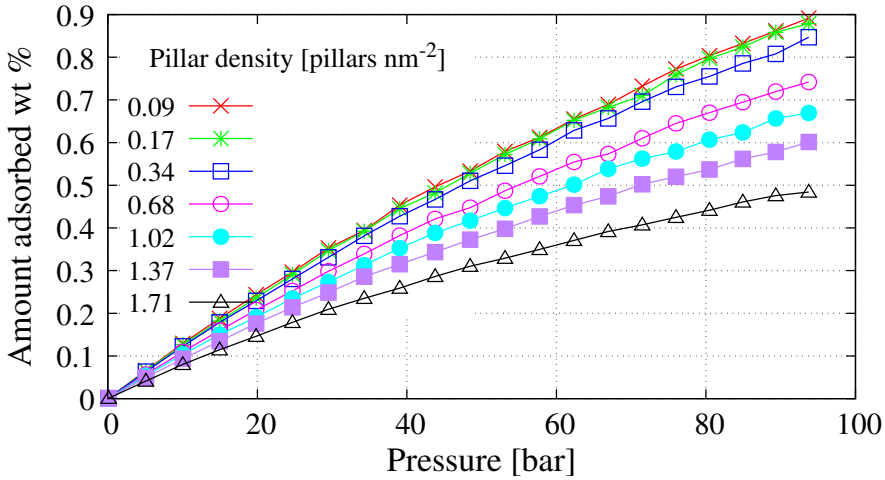

Figure 28: Gravimetric adsorption isotherms of H_2 at T= 298 K for pillar type 3.

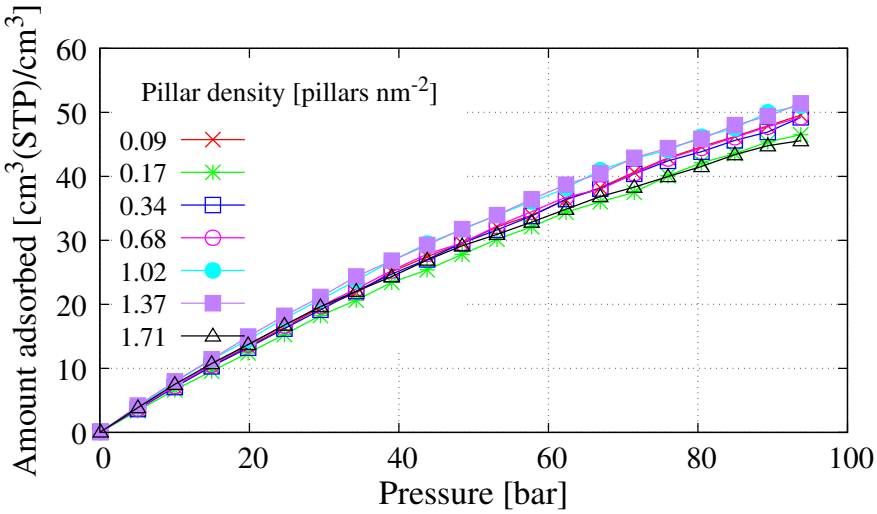

Figure 29: Volumetric adsorption isotherms of H_2 at T= 298 K for pillar type 3.

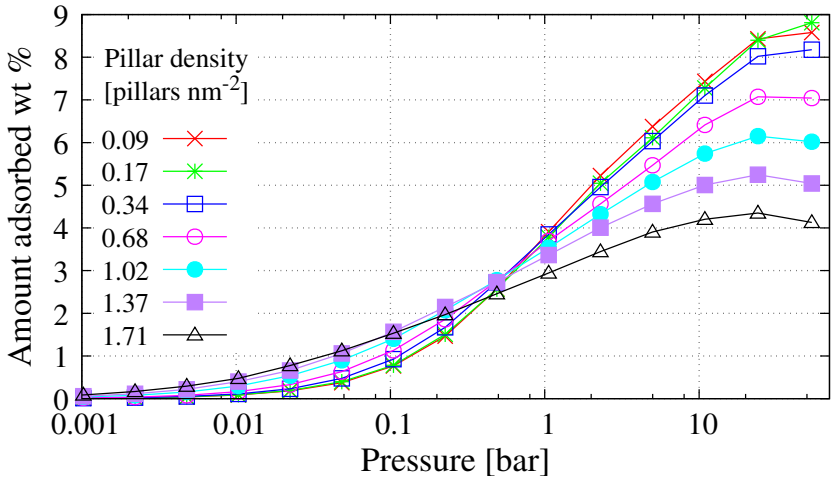

Figure 30: Gravimetric adsorption isotherms of H_2 at T= 77 K for pillar type 3.

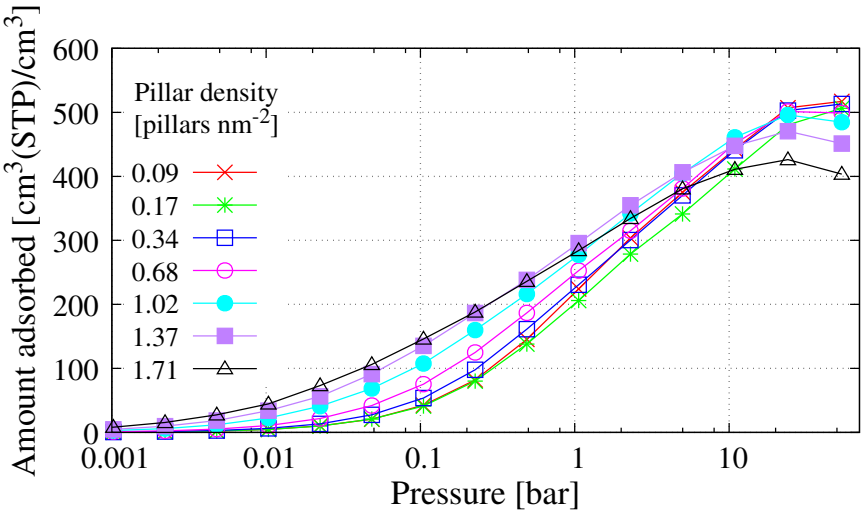

Figure 31: Volumetric adsorption isotherms of H_2 at T= 77 K for pillar type 3.

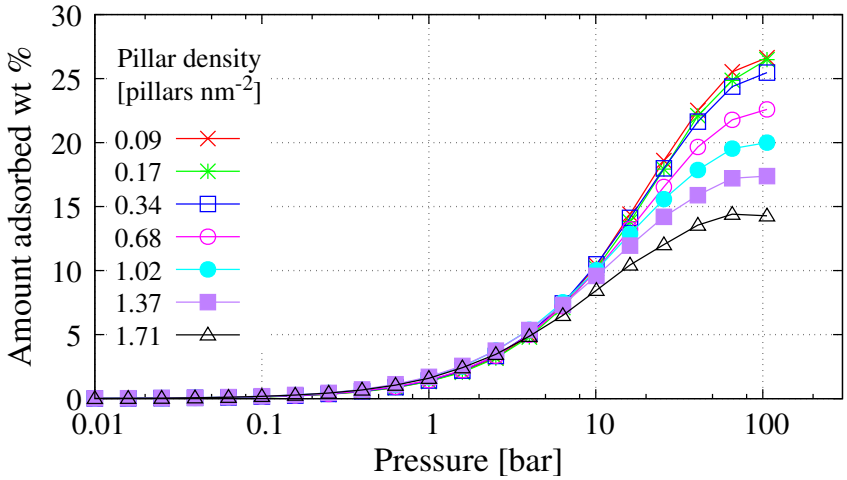

Figure 32: Gravimetric adsorption isotherms of N_2 at T= 298 K for pillar type 3.

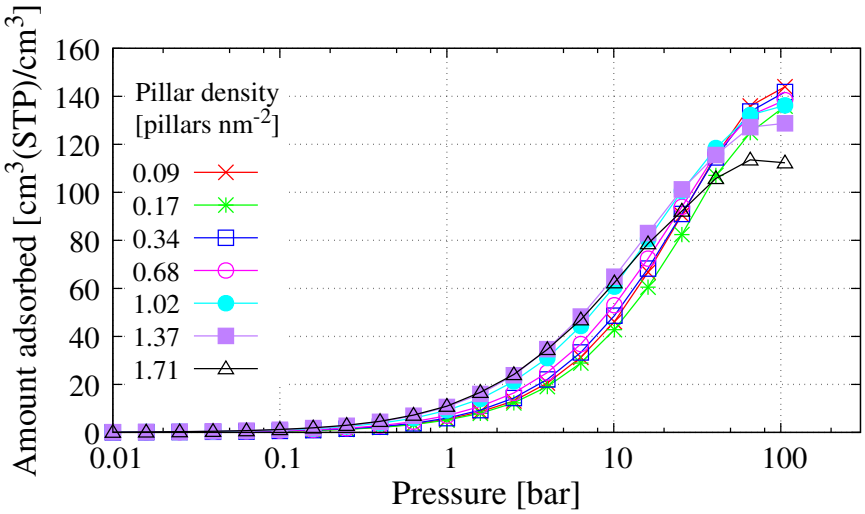

Figure 33: Volumetric adsorption isotherms of N_2 at T= 298 K for pillar type 3.

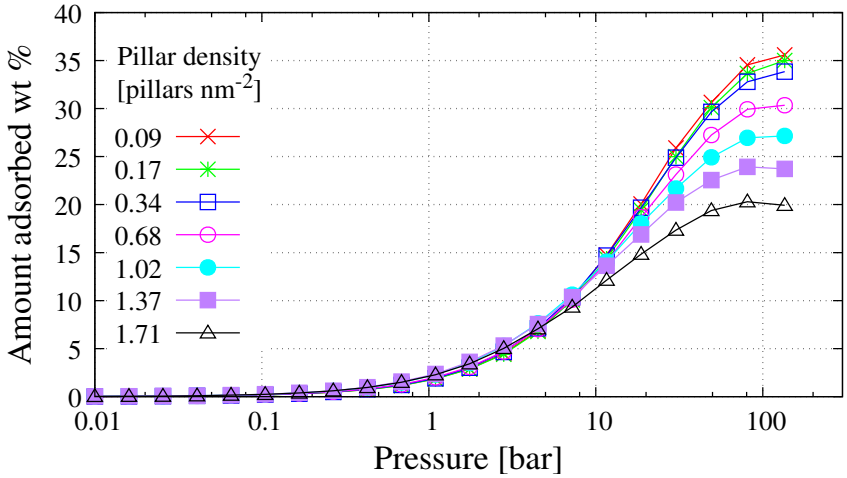

Figure 34: Gravimetric adsorption isotherms of O_2 at T= 298 K for pillar type 3.

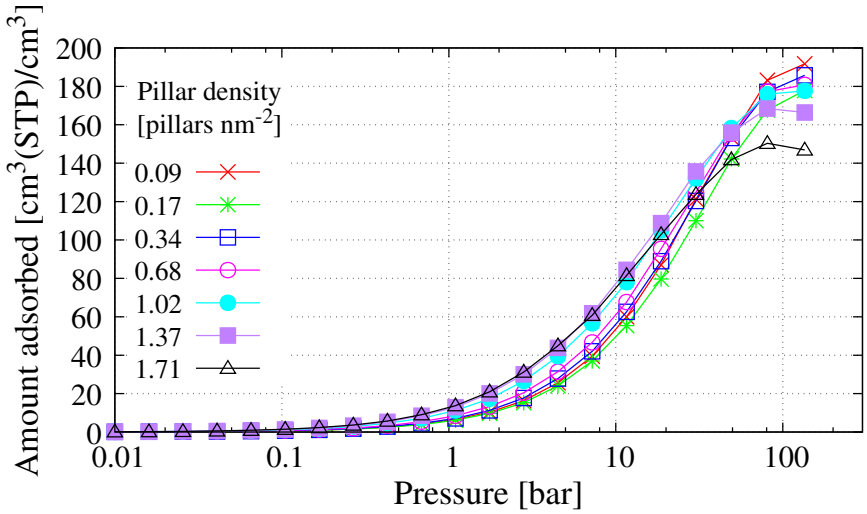

Figure 35: Volumetric adsorption isotherms of O_2 at T= 298 K for pillar type 3.

2.4. Pillar type 4

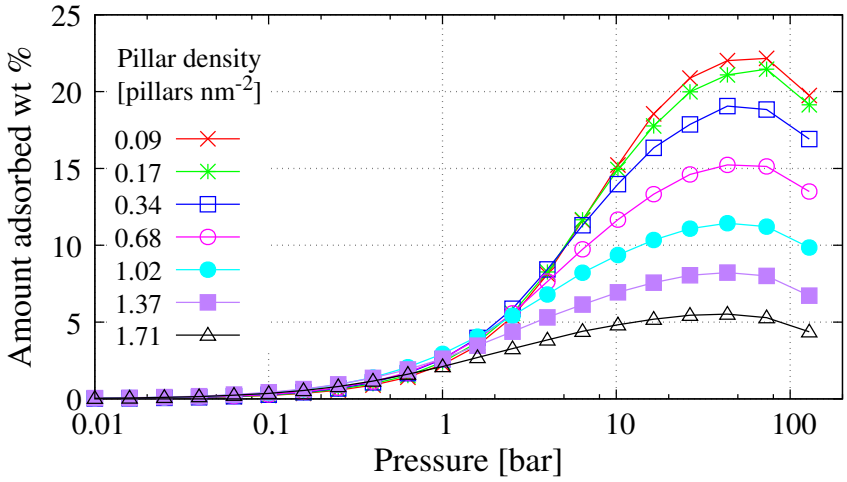

Figure 36: Gravimetric adsorption isotherms of CH_4 at T= 298 K for pillar type 4.

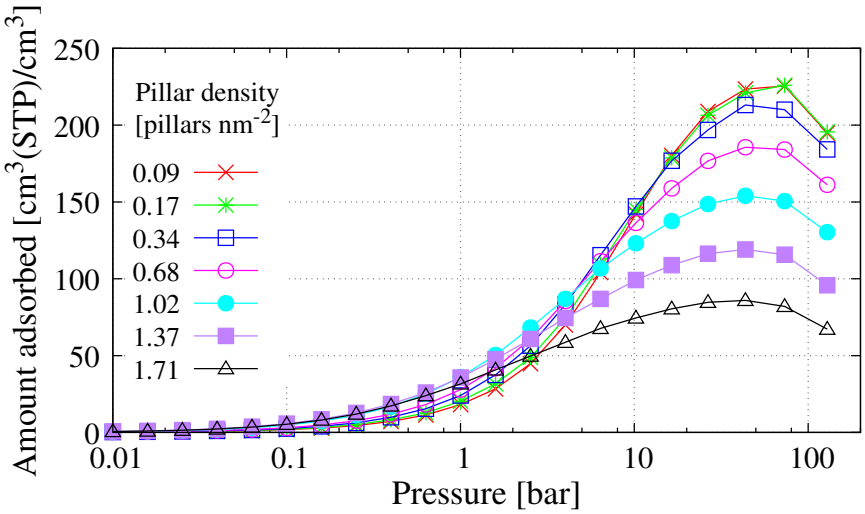

Figure 37: Volumetric adsorption isotherms of CH_4 at T= 298 K for pillar type 4.

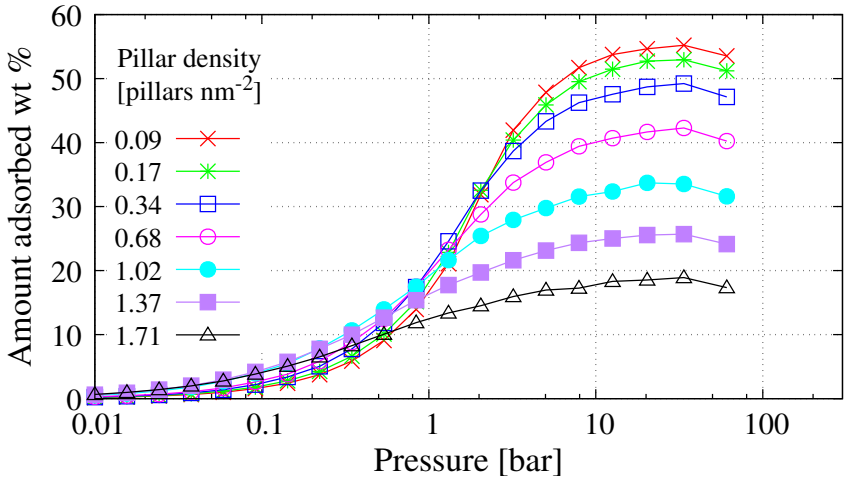

Figure 38: Gravimetric adsorption isotherms of CO_2 at T= 298 K for pillar type 4.

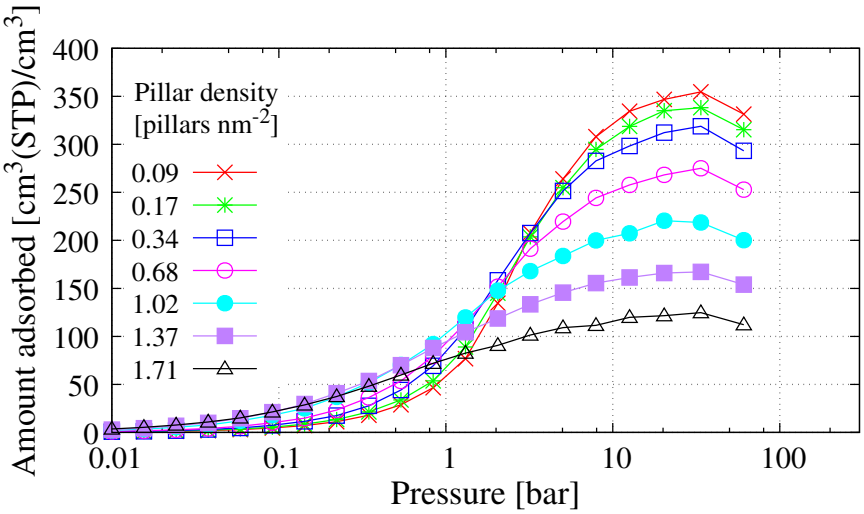

Figure 39: Volumetric adsorption isotherms of CO_2 at T= 298 K for pillar type 4.

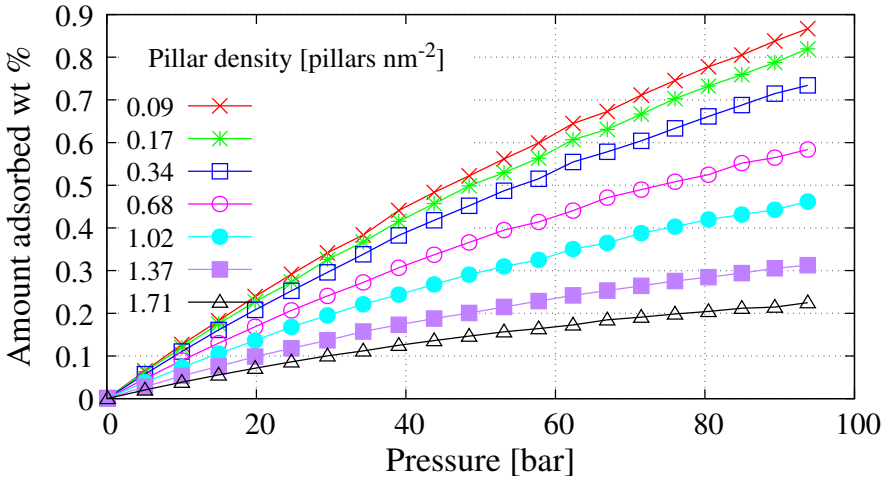

Figure 40: Gravimetric adsorption isotherms of H_2 at T= 298 K for pillar type 4.

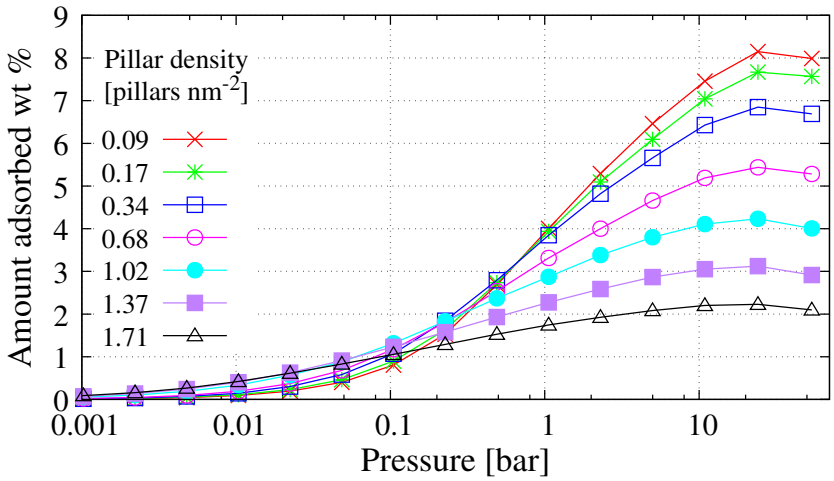

Figure 41: Gravimetric adsorption isotherms of H_2 at T= 77 K for pillar type 4.

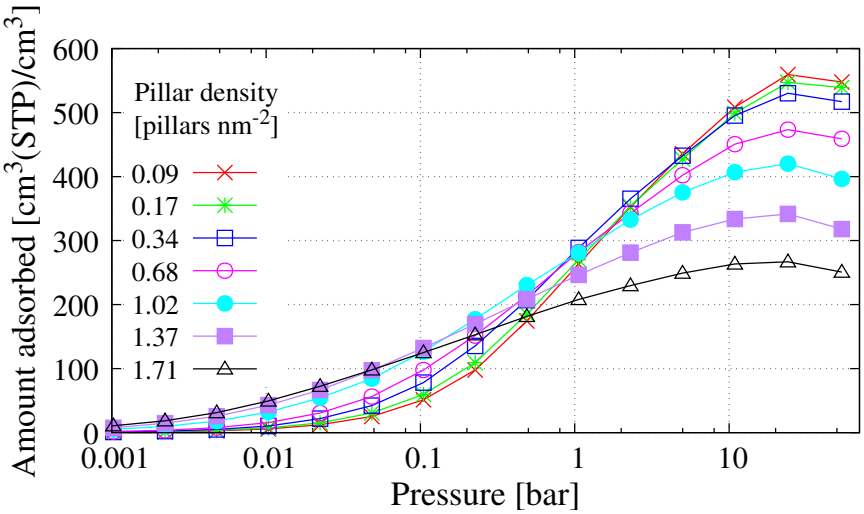

Figure 42: Volumetric adsorption isotherms of H_2 at T= 77 K for pillar type 4.

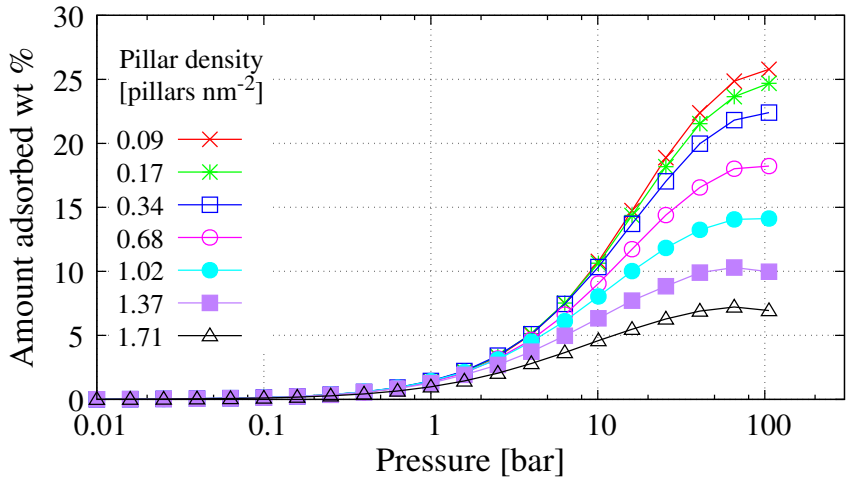

Figure 43: Gravimetric adsorption isotherms of N_2 at T= 298 K for pillar type 4.

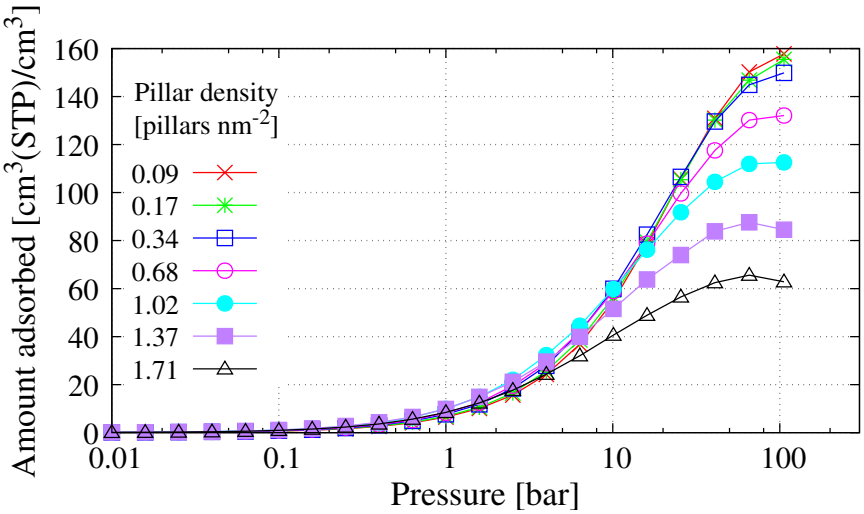

Figure 44: Volumetric adsorption isotherms of N_2 at T= 298 K for pillar type 4.

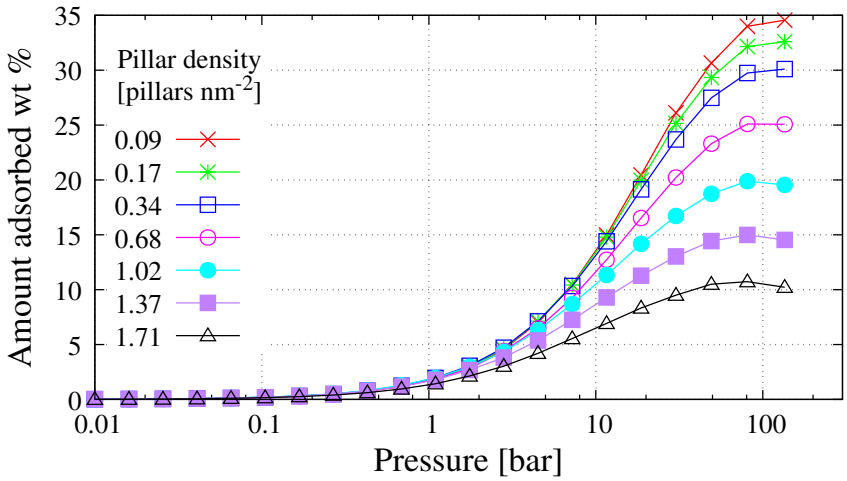

Figure 45: Gravimetric adsorption isotherms of O_2 at T= 298 K for pillar type 4.

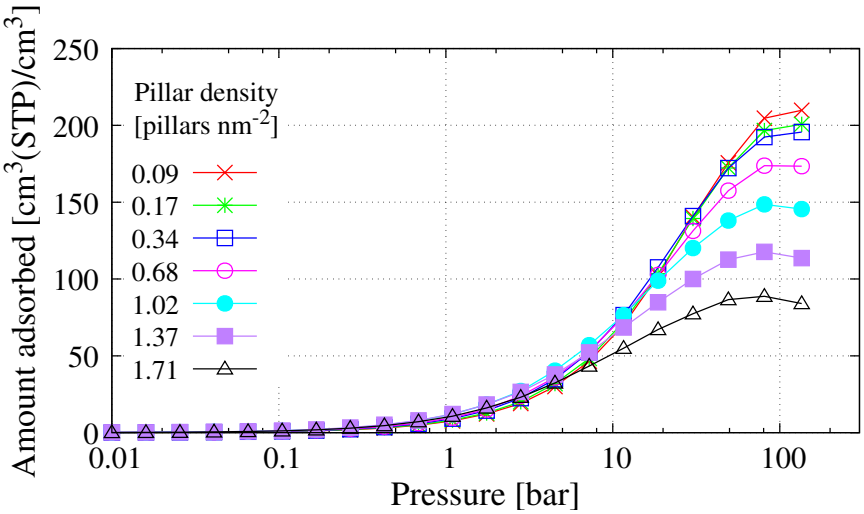

Figure 46: Volumetric adsorption isotherms of O_2 at T= 298 K for pillar type 4.

3. UFF vs DREIDING, Relative overstimation R

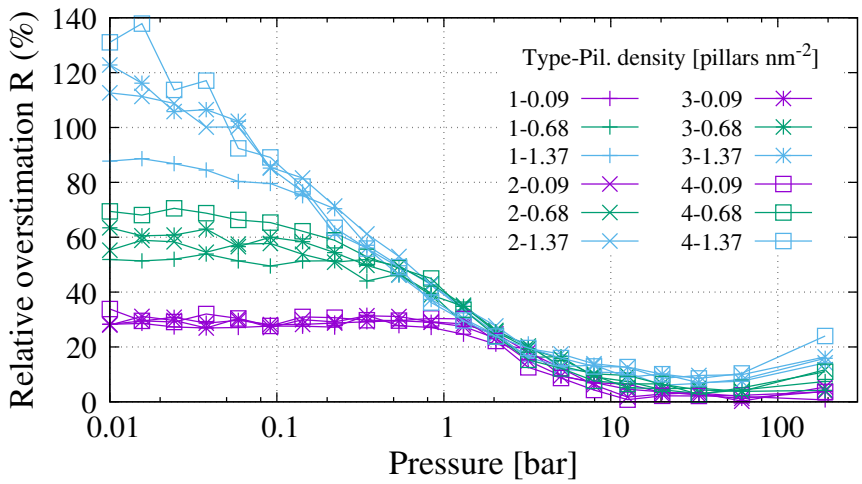

Figure 47: Relative overestimation R of CO_2 adsorption at 298 K using UFF force field in place of DREIDING force field.

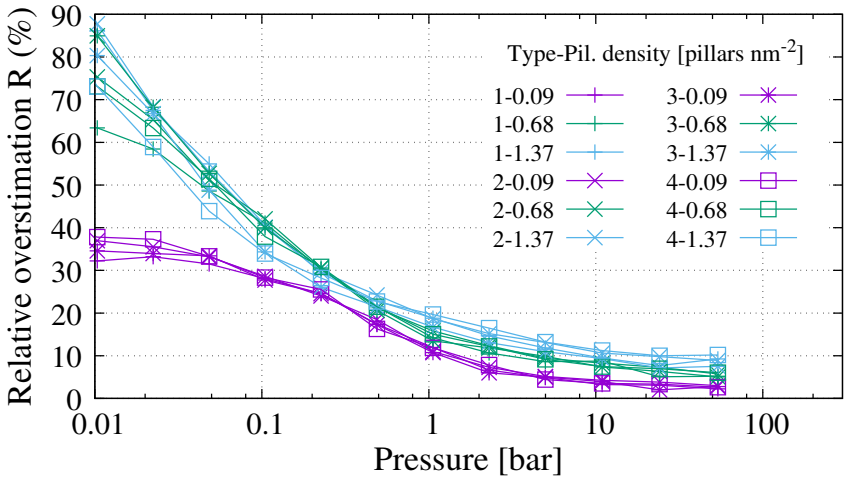

Figure 48: Relative overestimation R of H_2 adsorption at 77 K using UFF force field in place of DREIDING force field.

4. Selectivity (DREIDING)

4.1. Pillar type 1

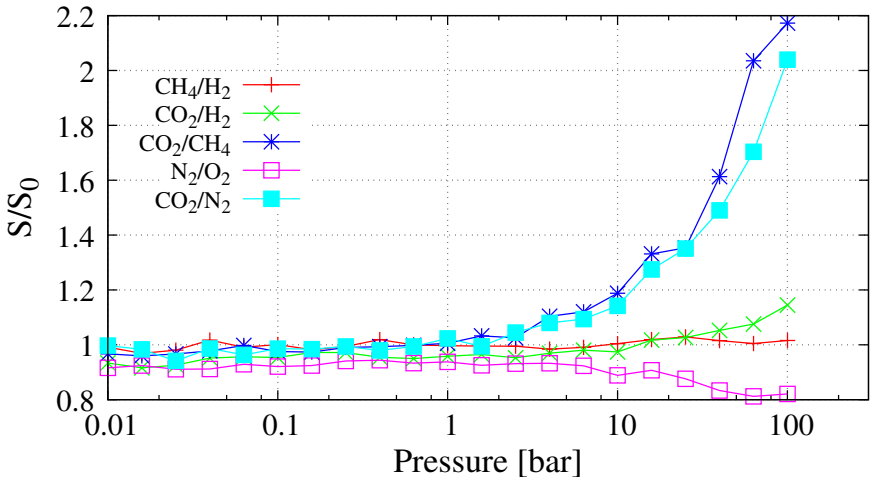

Figure 49: Selectivity for gas mixtures at T= 298 K, normalized with respect to the zero-pressure limit value of selectivity (S_0), for the sample with pillar type 1 and pillar density 0.09 pillars nm $^{-2}$.

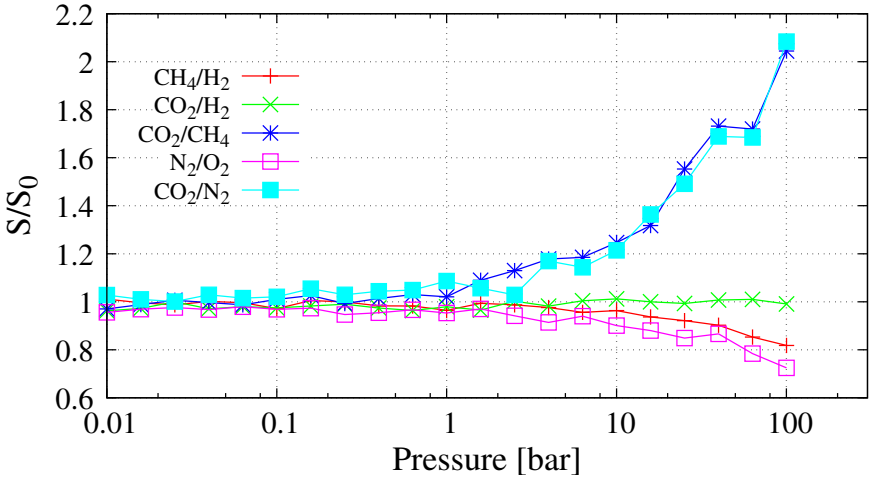

Figure 50: Selectivity for gas mixtures at T= 298 K, normalized with respect to the zero-pressure limit value of selectivity (S_0), for the sample with pillar type 1 and pillar density 1.37 pillars nm $^{-2}$.

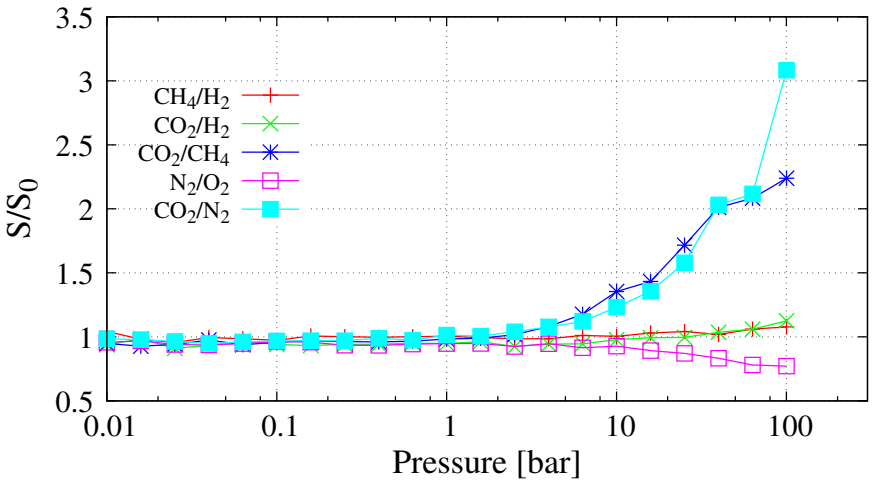

Figure 51: Selectivity for gas mixtures at T= 298 K, normalized with respect to the zero-pressure limit value of selectivity (S_0), for the sample with pillar type 4 and pillar density 0.09 pillars nm $^{-2}$.

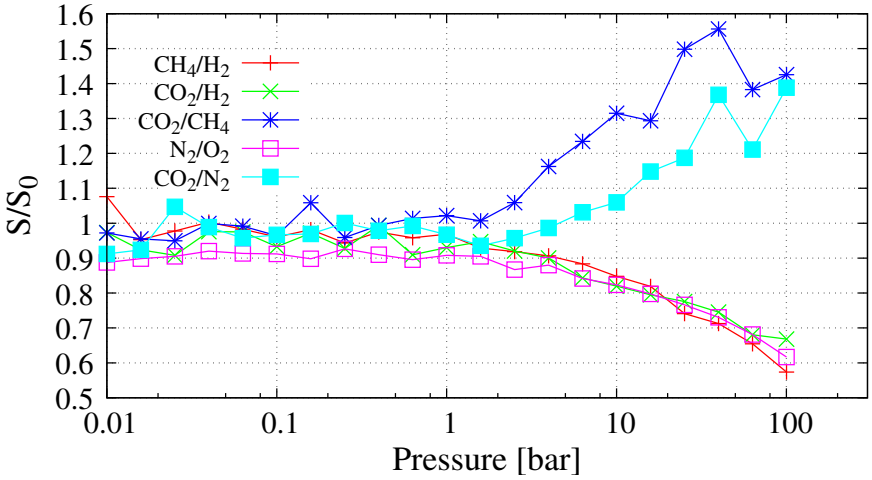

Figure 52: Selectivity for gas mixtures at T= 298 K, normalized with respect to the zero-pressure limit value of selectivity (S_0), for the sample with pillar type 4 and pillar density 1.37 pillars nm $^{-2}$.

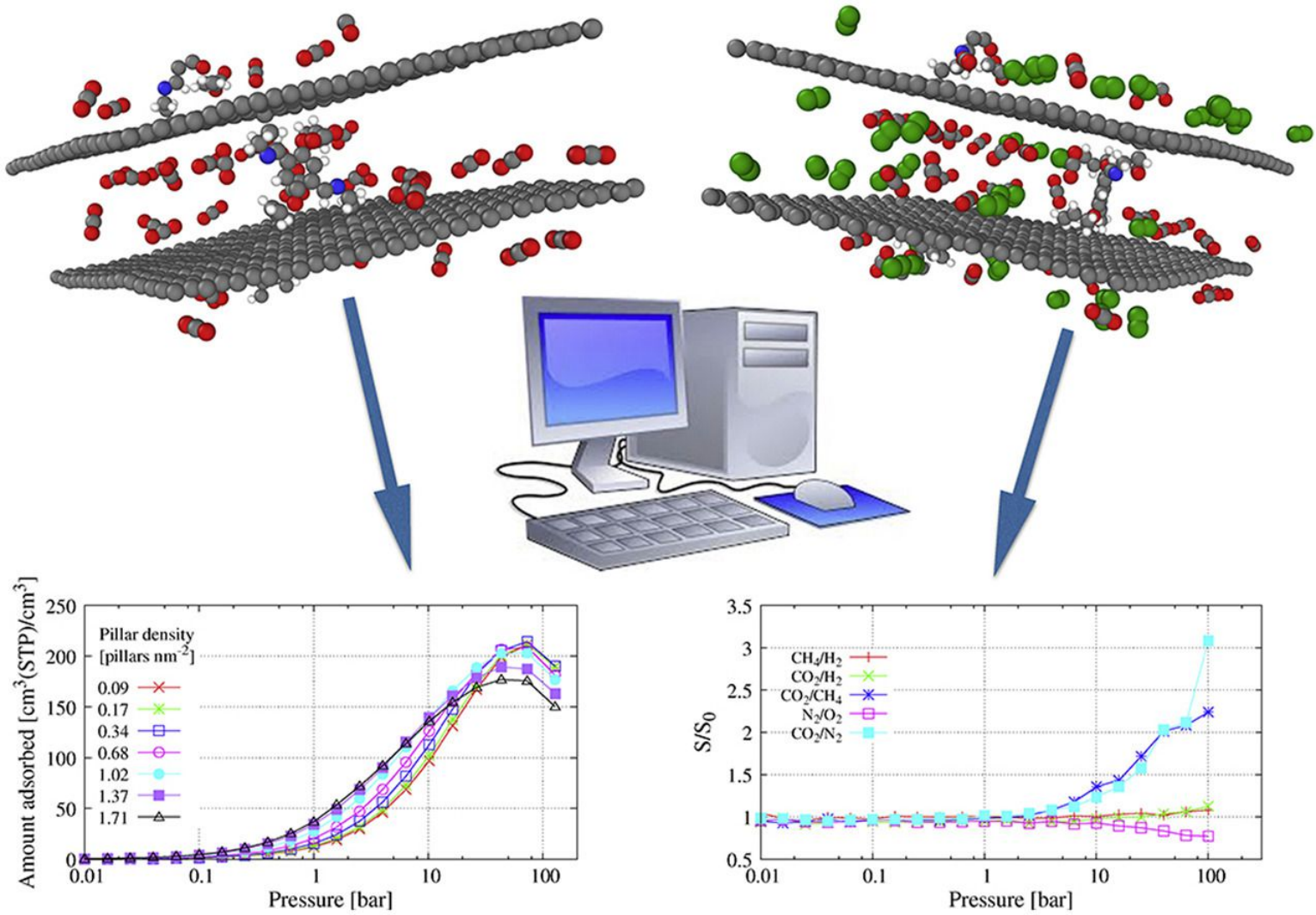
Pillar density
[pillars nm^{-2}]
0.09
0.17
0.34
0.68
1.02
1.37
1.71
Amount adsorbed [cm^3(STP)/cm^3]
Pressure [bar]
CH_4/H_2
CO_2/H_2
CO_2/CH_4
N_2/O_2
CO_2/N_2
S/S_0
Pressure [bar]